

ORIGINAL ARTICLE

A Dynamic Core Network and Global Efficiency in the Resting Human Brain

F. de Pasquale¹, S. Della Penna¹, O. Sporns², G. L. Romani¹ and M. Corbetta^{3,4}

¹Institute for Advanced Biomedical Technologies, Department of Neuroscience, Imaging and Clinical Sciences, “G. D’Annunzio” University, Chieti, Italy, ²Department of Psychological and Brain Sciences, Indiana University, Bloomington, IN, USA, ³Departments of Neurology, Radiology, Anatomy and Neurobiology, Washington University School of Medicine, Saint Louis, MO, USA and ⁴ITAB, University of Chieti, Chieti, Italy

Address correspondence to F. de Pasquale. Email: peppinodepa@gmail.com

Abstract

Spontaneous brain activity is spatially and temporally organized in the absence of any stimulation or task in networks of cortical and subcortical regions that appear largely segregated when imaged at slow temporal resolution with functional magnetic resonance imaging (fMRI). When imaged at high temporal resolution with magneto-encephalography (MEG), these resting-state networks (RSNs) show correlated fluctuations of band-limited power in the beta frequency band (14–25 Hz) that alternate between epochs of strong and weak internal coupling. This study presents 2 novel findings on the fundamental issue of how different brain regions or networks interact in the resting state. First, we demonstrate the existence of multiple dynamic hubs that allow for across-network coupling. Second, dynamic network coupling and related variations in hub centrality correspond to increased global efficiency. These findings suggest that the dynamic organization of across-network interactions represents a property of the brain aimed at optimizing the efficiency of communication between distinct functional domains (memory, sensory-attention, motor). They also support the hypothesis of a dynamic core network model in which a set of network hubs alternating over time ensure efficient global communication in the whole brain.

Key words: betweenness centrality, brain dynamics, core network model, MEG, resting-state networks

Introduction

In the resting state, that is, in the absence of any stimulation or overt behavior, spontaneous brain activity is spatially and temporally structured in networks of cortical and subcortical regions (so-called resting-state networks, RSNs) that were originally observed with functional magnetic resonance imaging (fMRI) (Biswal et al. 1997). Although RSNs appear largely segregated in fMRI [but see Hutchison et al. (2013)] and their topography is relatively stable during task performance (Biswal et al. 1997; Friston 2002; Beckmann et al. 2005; Damoiseaux et al. 2006; Dosenbach et al. 2007; Smith et al. 2009; Cole et al. 2014), they must interact during task and rest through several neurophysiological mechanisms including band-limited signal coherence at fast time scale or band-limited power (BLP) envelope correlation at slower

time scales (seconds to minutes) (Engel et al. 2013). This idea is supported by a growing number of EEG/MEG/ECOG studies (He et al. 2008; Nir et al. 2008) that have identified different frequency-specific correlates of fMRI-RSNs, as well as mechanisms of their interaction (de Pasquale et al. 2010; Brookes, Woolrich, et al. 2011; de Pasquale et al. 2012; Hipp et al. 2012; Betti et al. 2013; Marzetti et al. 2013). Electrophysiological RSNs therefore provide a model to study functional segregation and integration in the brain (Bullmore and Sporns 2009; Tomasi and Volkow 2010). One MEG correlate of fMRI RSNs is the coupled fluctuation of BLP in alpha/beta frequency band between different RSN nodes (de Pasquale et al. 2010; Brookes, Woolrich, et al. 2011; de Pasquale et al. 2012; Hipp et al. 2012; Betti et al. 2013). The strength of BLP correlation between different brain regions varies

over time, with periods of strong correlation between nodes of the same network alternating with periods of weak or no correlation (de Pasquale et al. 2010, 2012). Furthermore, in a particular brain network, the Default Mode Network (DMN), periods of strong within-network correlation correspond to periods of stronger interactions with other regions/networks (de Pasquale et al. 2012). This suggests that DMN, and some of its main nodes such as the posterior Cingulate Cortex (pCC), may function as a dynamic hub for across-network interaction (de Pasquale et al. 2012; Engel et al. 2013). This nonstationary coupling (within/across networks) has been related to the formation of brain states (Hutchison et al. 2013), fluctuations of internal noise or cognitive states (Shirer et al. 2012), scale-free dynamics (Van de Ville et al. 2010), and the global workspace model (Dehaene and Naccache 2001). The idea that some regions are more central than others in the brain's network is also suggested by studies on the architecture of structural and functional connections (Buckner et al. 2009; Honey et al. 2009; Cole et al. 2010; Doucet et al. 2011; Hacker et al. 2013; Power et al. 2013), with a number of different models proposed including small-worldness (Achard and Bullmore 2007), network cores (Shanahan 2012; Bassett et al. 2013), and rich club organization (van den Heuvel and Sporns 2013). While theoretical arguments have been put forward to explain the advantage of certain functional architectures, no clear explanation exists today for the nonstationarity of brain interactions nor the functional role of hubs in the brain.

In this paper, we extend our analysis on the dynamics of cortical interactions in the resting state by testing the hypothesis that network centrality and nonstationarity of coupling are closely related to the efficiency of communication. To this end, we apply graph theory measures to MEG BLP coupling to characterize network topology in terms of centrality, efficiency, and modularity (Buckner et al. 2009; van den Heuvel and Sporns 2013). We then relate the temporal dynamics of these quantities to RSNs' nonstationary coupling. Our findings show a close relationship between the dynamics of RSNs coupling and efficiency of communication and identify a set of cortical regions that function as dynamic hubs for integrating different networks.

Materials and Methods

Subjects and Acquisition Procedures

A total of 13 healthy young adult subjects (mean age 29 ± 6 years, 5 females), same sample as in de Pasquale et al. (2012), were scanned with MEG at rest. During the acquisition (3 runs per subject, 5 min each), subjects maintained fixation on a small visual target. Neuro-magnetic signals (filter settings 0.16–250 Hz, 1 KHz sampling rate) were recorded using the 153-magnetometer MEG system developed and installed at the University of Chieti (Della Penna et al. 2000).

MEG Analysis Pipeline

A full description of our analysis pipeline to obtain BLP time series can be found in de Pasquale et al. (2010, 2012) and Mantini et al. (2011). Here we summarize the basic steps reported in Figure 1. First, environmental and physiological (e.g., cardiac, ocular) artifacts were removed from sensor-space MEG time series using an ICA-based approach. Following ICA separation, only ICs that were not artifact were retained for further analysis. However, if the number of nonartifact ICs was <4 , possibly indicating excessive movements of the head, the whole run was eliminated. This step reduced the number of runs analyzed in this study to

27. Then, source-space signals were reconstructed on a 3D Cartesian grid (64 mm^3 cubic voxels) using a Weighted Minimum Norm Least Square (WMNLS) estimation of the nonartifactual IC sensor maps. For every voxel in the 3D grid, the MEG activity is represented by a current dipole with 3 components. We selected the orientation of the current dipole as free (and not perpendicular to the cortex surface), because the voxel volume might include parts of gyri with a small curvature radius and a single direction perpendicular to the cortex could not be defined. Notably, the size of the voxel matched the typical MEG spatial resolution (~ 5 mm). We assumed that nodes of different RSNs correspond to single MEG voxels. Since the diagonal of our cubic voxel is around 7 mm, the volume of each node is comparable to that of typical ROIs used in fMRI analysis [10 mm spheres, see Stanley et al. (2013)]. The individual 3D grid was then projected into the MNI 152 atlas space, so that every voxel centroid was assigned a set of MNI coordinates. The 3 components of the MEG activity were obtained at each voxel from the linear combination of IC time courses weighted by the corresponding source maps. To reduce the computational burden of the dynamic analyses, we focused on 42 core nodes of 6 RSNs: the Default Mode (DMN), Dorsal and Ventral Attention (DAN and VAN), Motor (MOT), Visual (VIS), and Language (LAN) network (de Pasquale et al. 2012) (see Table 1 for a list of abbreviations and MNI coordinates). Additionally, we concentrated on network coupling in the β band [14–25 Hz], in which several prior studies have reported a similarity between BLP temporal correlation maps and fMRI RSN topography (Brookes, Woolrich et al. 2011; de Pasquale et al. 2012; Hipp et al. 2012). Therefore, source-space signals were filtered in this band and source-space power time series were estimated over 400 ms windows sliding every 20 ms to cover the entire resting-state run. Transient coupling across nodes was estimated through Pearson coefficient over a time window lasting 10 s and sliding every 200 ms. A time window of 10 s corresponds to the carrier frequency at which BLP time series correlation most strongly occur (~ 0.1 Hz) (de Pasquale et al. 2010; Hipp et al. 2012).

Test for Nonstationary Coupling

To formally assess the nonstationarity of the functional coupling, we implemented the methodology proposed in Chang and Glover (2010) and Zalesky et al. (2014). Due the computational burden, here we present a case study based on 1 subject. We proceeded as follows. First, by means of the Bayesian Information Criterion (BIC), we estimated the order of a Vector Auto Regressive (VAR) model to fit our BLP data. We selected the BLP time series extracted from all the 42 nodes over all the runs analyzed in this study. Then, we fitted a VAR model letting the model order vary in the range [1, 500]. For each node and model order, we computed BIC and we averaged it across the considered nodes. Then, once the model order of the VAR had been estimated, we produced surrogate BLP data as suggested in Chang and Glover (2010). Since this step is extremely computationally expensive, we selected, for 1 run of 1 subject, the nodes belonging to the proposed functional core: pCC, L SMA, L/R pIPS, and 1 node for each of the remaining RSNs, namely L STS, R MFG, and R V7. For these nodes, we formally tested the nonstationarity of their connections (see SI for a detailed description). As described in (Chang and Glover 2010), we generated 1000 bootstrap replicates of each BLP time series and then computed their nonstationary coupling as in the real data. Then, for each surrogate connection, we computed the univariate test statistics proposed in Zalesky et al. (2014). This statistics applied on the bootstrap is based on

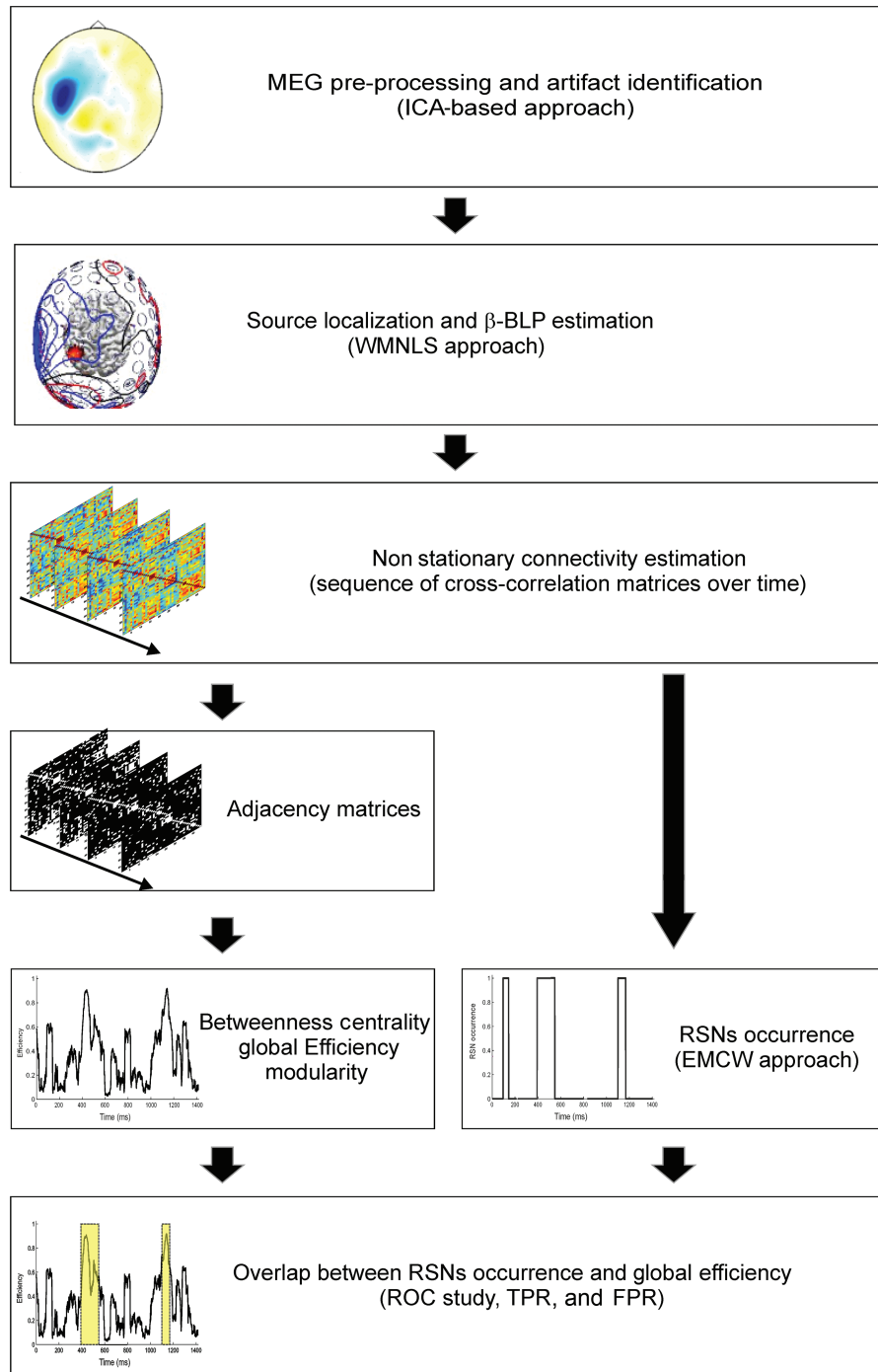


Figure 1. Analysis pipeline. Outline of the analysis pipeline, see Materials and Methods.

the idea given the time course of a connection, quantified through the Pearson correlation coefficient, the longer and larger are the excursions observed from its median value, and the greater is the evidence for nonstationary behavior. The computation of this statistics applied on the bootstrap sample provides a null distribution. From this distribution, we estimated the 95th percentile that will represent the threshold adopted to perform the test on real connections, that is, if the statistics obtained from the real connection is above this threshold, we can reject the null hypothesis that such connection is stationary at a

significance level of $\alpha = 0.05$. Thus, each connection exceeding its threshold can be considered as statistically nonstationary.

Epoch Labeling for RSN Coupling

MEG RSNs are patently nonstationary, and nonstationary connections can be formally demonstrated (see previous section). Thus, to characterize dynamic properties of RSNs, we defined temporal windows in which each network showed high internal coupling through an algorithm validated in previous studies [the

Table 1 List of abbreviations adopted in the paper and MNI coordinates of the 42 considered nodes

Common names	Abbreviation	MNI coordinates	Common names	Abbreviation	MNI coordinates
Dorsal Attention Network	DAN		Visual Network	VIS	
Left posterior intra parietal sulcus	L pIPS	(-25, -67, 48)	Left area V1	L V1	(-3, -101, -1)
Right posterior intra parietal sulcus	R pIPS	(23, -69, 49)	Right area V1	R V1	(11, -88, -4)
Left frontal eye field	L FEF	(-26, -12, 53)	Left area v2 dorsal	LV2d	(-8, -99, 7)
Right frontal eye field	R FEF	(30, -13, 53)	Right area V2 dorsal	R V2d	(14, -96, 13)
Left middle temporal	L MT	(-43, -72, -8)	Left area V3	L V3	(-9, -96, 13)
Right middle temporal	R MT	(42, -70, -11)	Right area V3	R V3	(20, -95, 18)
Ventral Attention Network	VAN		Left area V4	L V4	(-31, -77, -17)
Right middle frontal gyrus	R MFG	(41, 17, 31)	Right area V4	R V4	(27, -71, -14)
Right pre-central sulcus	R PCS	(41, 2, 50)	Left area V7	L V7	(-23, -78, 26)
Right supramarginal gyrus	R SMG	(52, -48, 28)	Right area V7	R V7	(32, -78, 25)
Right superior temporal gyrus	R STG	(58, -48, 10)	Motor Network	MOT	
Right ventral frontal cortex	R VFC	(40, 21, -4)	Left second somatosensory	L S2	(-60, -28, 24)
Default Mode Network	DMN		Right central sulcus	R CS	(35, -26, 55)
Left angular gyrus	L AG	(-43, -76, 35)	Left central sulcus	L CS	(-37, -19, 53)
Right angular gyrus	R AG	(51, -64, 32)	Right second somatosensory	R S2	(57, -28, 23)
Posterior cingulate/precuneus	pCC	(-3, -54, 31)	Left supplementary motor area	L SMA	(-1, -17, 55)
Ventral medial prefrontal cortex	L mPFC	(-2, 51, 2)	Right supplementary motor area	R SMA	(4, -15, 53)
Dorso medial prefrontal cortex	L mPFC2	(-13, 52, 23)	Left putamen	L PUT	(-30, -18, 10)
Right medial prefrontal cortex	R mPFC	(2, 53, 24)	Right putamen	R PUT	(30, -17, 9)
Left inferior temporal gyrus	L ITG	(-57, -25, -17)	Language Network	LAN	
			Left dorsal inferior frontal gyrus	L dIFG	(-44, 23, 15)
			Left superior temporal sulcus	L STS	(-50, -54, 22)
			Anterior superior temporal gyrus	T1a	(-56, -12, -3)
			Upper part of the Pars opercularis of the inferior frontal gyrus	F3opd	(-44, 21, 24)
			Pars triangularis opercularis of the inferior frontal gyrus	F3tv	(-43, 20, 4)
			Posterior superior temporal gyrus	T1p	(-55, -48, 15)

Extended Maximum Correlation Windows, EMCWs, algorithm, see [de Pasquale et al. \(2010, 2012\)](#). The objective of this algorithm is to identify epochs in which the contrast between within-network and external-to-network correlation is maximal. This was accomplished using an iterative strategy based on Old Bachelor Acceptance thresholding ([Hu et al. 1995](#)) in which a subset of nodes from each considered RSN is input to the algorithm together with an external node used as a reference. The search for epochs in which the least within-network correlation is above a threshold while the correlation between the seed and 1 external node is minimal was repeated for different sets of nodes. All epochs obtained for different sets of nodes belonging to the same RSN were then concatenated in a network-specific set of EMCWs called INSIDE-RSN, for example, “INSIDE-DMN” and so on. The remaining epochs were then concatenated in a set called OUTSIDE-RSN, for example, “OUTSIDE-DMN.” In these periods, we assumed either partial or no internal coupling of the network. All these epochs were then used to compute z-score matrices INSIDE- and OUTSIDE-RSN [see SI for z-score computation and [de Pasquale et al. \(2012\)](#) for further details]. Additionally, the same epoch labeling was used to examine differences in both local and global properties of integration in the brain (e.g., betweenness centrality or global efficiency) (see below).

Graph Analyses

To characterize the architecture of network interactions in terms of centrality, modularity, and efficiency, we adopted 2 sets of graph theory measures. First, we considered interactions averaged across epochs of high or low/partial network coupling (i.e.,

INSIDE- or OUTSIDE-RSN). Then, z-score interaction matrices computed INSIDE and OUTSIDE-RSNs epochs were thresholded to obtain adjacency matrices for graph measures. First, a threshold accounting for leakage effects was applied [see SI and [de Pasquale et al. \(2012\)](#) for details]. Then, for each z-score interaction matrix, we computed the number of graph components as a function of different thresholding values. The threshold for each matrix was estimated as the highest value that maintained the graphs fully connected (i.e., the number of components is equal to the number of nodes).

To characterize local properties of graph nodes, we adopted the binary betweenness centrality (BC) that is related to the number of times a node acts as a bridge between the strongest connections of any 2 nodes. Thus, nodes with high values of BC participate in a large number of shortest paths. For each z-score interaction matrix computed INSIDE/OUTSIDE-RSNs epochs, BC is estimated according to the following formula:

$$BC(v) = \frac{2}{(N-1)(N-2)} \sum_{i \neq j \neq v} \frac{\sigma_{ij}(v)}{\sigma_{ij}} \quad (1)$$

where σ_{ij} is the total number of shortest paths from node i to node j , $\sigma_{ij}(v)$ is the fraction of those paths passing through v , and N is the graph order ([Rubinov and Sporns 2010; Sporns 2011](#)). To compare the pattern of BC values across different z-score matrices, equation (1) was normalized to the sum of BC across nodes. To assess the significance of the BC, a threshold was obtained as the average BC (estimated with the same procedure as above) from a population of 1000 random graphs preserving the node degree distribution, see [Maslov and Sneppen \(2002\)](#).

To characterize the global integration properties of the graph, we adopted the Global Efficiency (GE), a measure related to information exchange. The parameter GE, given our graph edges are defined in terms of connectivity strength, will reflect the efficiency of the interaction across the whole graph (Rubinov and Sporns 2010; Sporns 2011). GE is defined as the average inverse shortest path length in the network, which is inversely related to the characteristic path length:

$$GE = \frac{1}{N[N-1]} \sum_{i,j \in N, i \neq j} \frac{1}{d_{ij}} \quad (2)$$

where d_{ij} is the shortest path between nodes i and j . GE was estimated as a function of the threshold, INSIDE and OUTSIDE-RSNs epochs.

Second, we followed the dynamics of interactions over time. To this aim, we obtained graph edges from a series of 40 500 cross-correlation matrices (see Fig. 1). All graph parameters were estimated dynamically every 200 ms, run by run separately, and each run was treated as an independent observation. This choice does not separate sources of variances between runs and subjects but is consistent with other strategies of analysis, for example, spatial ICA, in which MEG time courses from different runs and subjects are concatenated together (Brookes, Hale, et al. 2011; Brookes, Woolrich, et al. 2011). To analyze the dynamics of the RSN interactions, we could not adopt the same statistics based on z-scores, since these were obtained by averaging across specific time epochs and this would not allow us to track our parameters over time. Furthermore, we could not base our threshold on the fully connectedness of the sequence of graphs. This would have provided us with the lowest correlation value corresponding to the time in which the graph showed the lowest coupling. In this way, time instances of strong and low coupling could not be distinguished and connections of different intensities would have been treated as the same. Therefore, we assumed a criterion based on the highest on average graph centrality (we obtained $r = 0.6$ as a threshold, see Results). To identify this value, we first estimated BC as a function of time and the binary threshold. For each threshold, the binary matrices obtained after thresholding, at every time $t \in [0, 0.2, \dots, 290]$ s of every 5-min run, we computed the BC as a function of time:

$$BC(v, t) = \frac{2}{(N-1)(N-2)} \sum_{i \neq j \neq v} \frac{\sigma_{ij}(v, t)}{\sigma_{ij}(t)} \quad (3)$$

where $\sigma_{ij}(t)$ is the total number of shortest paths from node i to node j at time t , $\sigma_{ij}(v, t)$ is the number of those paths passing through v at time t . Then, we averaged across time the node BC estimated at every time point of every run and every subject as a function of the threshold ranging between [0 1]. After averaging the BC across nodes, the threshold corresponding to the maximum was selected, and the correlation matrices were thresholded to estimate the binary GE as a function of time as:

$$GE(t) = \frac{1}{N(N-1)} \sum_{i,j \in N, i \neq j} \frac{1}{d_{ij}(t)} \quad (4)$$

where $d_{ij}(t)$ is the shortest path between nodes i and j estimated over the binary correlation matrix at time t . Finally, to check that the observed GE values were not inflated by the presence of a few hubs, we computed the graph modularity by means of the Lovain algorithm for undirected graphs (Blondel et al. 2008). All the above-defined quantities have been estimated by means of the

MATLAB toolbox, Brain Connectivity Toolbox (BCT) (<https://sites.google.com/site/bctnet/>) (Rubinov and Sporns 2010). For the graph visualization, we used the MATLAB toolbox VISUALCONNECTOME (Dai and Huiguang 2011) (<http://code.google.com/p/visualconnectome/>).

Receiver Operating Characteristic Estimation

To investigate the relationship between RSN occurrence, that is, epochs of strong within-network coupling and global efficiency, we treated every network as a binary classifier of periods of high efficiency whose performance can be assessed in terms of receiver operating characteristic (ROC) analysis (see Fig. 1). We proceeded as follows: for every run, we computed the mean value of the timeseries {GE}. Then, to identify periods of high efficiency, we binarized this time series above its mean to obtain {BGE}. We adopted the mean as a threshold since we were not interested in the exact location of the local GE maxima but more in the temporal extension of periods of high efficiency. For simplicity of notation, in what follows we will refer to these periods of high efficiency as “efficiency peaks.” Analogously, for every network, we computed a binary time series {BN} in which the ones corresponded to the location and extension of every INSIDE-RSN epoch. Thus, the True (TP) and False Positives (FP), True (TN), and False Negatives (FN) were defined in terms of the following logical operations:

$$\begin{aligned} TP &= BN \cap BGE \text{ (presence of INSIDE - RSN epoch and} \\ &\quad \text{efficiency peak)} \\ TN &= (\neg BN) \cap (\neg BGE) \text{ (absence of INSIDE - RSN epoch} \\ &\quad \text{and efficiency)} \\ FP &= BN \cap (\neg BGE) \text{ (presence of INSIDE - RSN epoch and} \\ &\quad \text{absence of efficiency peak)} \\ FN &= (\neg BN) \cap BGE \text{ (absence of INSIDE - RSN epoch} \\ &\quad \text{and presence of efficiency peak)} \end{aligned}$$

Based on these quantities, the true positive rate (TPR) and false positive rate (FPR) were computed as:

$$TPR = \frac{TP}{TP + FN}, \quad FPR = \frac{FP}{TN + FP} \quad (5)$$

so that every run provided a point in the plot (TPR, FPR) of the ROC. It must be stressed that this measure takes into account not only the simultaneous presence of INSIDE-RSN epochs and efficiency peaks but also their temporal extension. Finally, to fit the TPR, we used the model:

$$TPR = FPR^a - \frac{e^{-b \cdot FPR}}{e^{-b}} + c \quad (6)$$

where $[a, b, c]$ are parameters to be estimated (de Pasquale et al. 2004). Of note, the case $[1, 0, 1]$ corresponds to the bisecting line, that is, the chance level for a ROC. The fitting procedure was performed using the Levenberg-Marquardt algorithm for nonlinear least squares (Seber and Wild 2003).

Results

Network Coupling and BC

The centrality of RSN nodes was characterized in terms of BC estimated from Z-score connectivity matrices in the β band either inside (Fig. 2A—INSIDE-DMN) or outside (Fig. 2A—OUTSIDE-DMN)

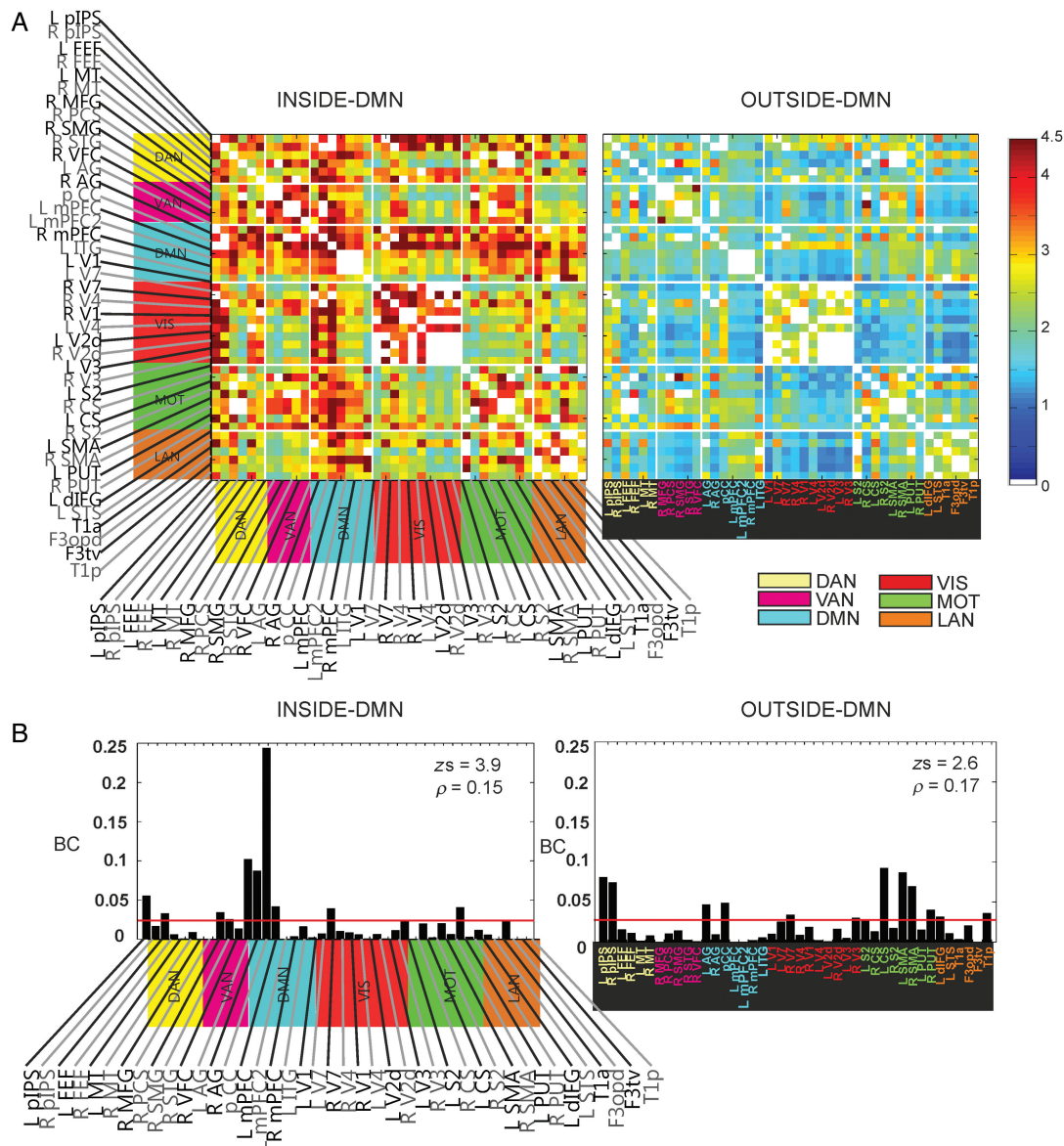


Figure 2. DMN centrality and nonstationarity. (A) z -score-based connectivity matrices computed INSIDE/OUTSIDE-DMN epochs for the DAN (yellow), VAN (purple), DMN (cyan), VIS (red), MOT (green), and LAN (brown). (B) Binary BC computed INSIDE/OUTSIDE-DMN epochs. The average BC computed in a set of equivalent random graphs is shown in red. Nodes of the DMN stand out as highly central during DMN INSIDE epochs while nodes from other networks emerge as central outside these epochs. Notably, these results are obtained at similar graph densities ($\rho = 0.15$ INSIDE- and $\rho = 0.17$ OUTSIDE-DMN).

epochs of strong internal coupling of the DMN (see Materials and Methods and SI for details). Inspection of the connectivity matrices suggests that cross-network interactions were overall stronger when the DMN was internally coupled (INSIDE-DMN). Furthermore, some networks, in descending order of strength DMN, DAN, and MOT, show stronger cross-network interactions than other networks (VAN, VIS, LAN) (Fig. 2A). To obtain the normalized BC (Fig. 2B), these matrices were thresholded corresponding to the maximum value that maintains the graph fully connected for the different epochs (see Materials and Methods for details). These thresholds, as shown in [Supplementary Figure 1A and B](#), were stronger in INSIDE ($z = 3.9$) than OUTSIDE ($z = 2.6$) DMN epochs, a result consistent with our previous work ([de Pasquale et al. 2012](#)). When the DMN coupling is strong (INSIDE-DMN epochs), DMN nodes are central (Fig. 2B), and this property is robust with respect to the choice of the threshold, as proved

by the centrality rank (this step is described in SI and reported in [Supplementary Fig. 1C](#)). In the bar plot of Figure 2B, BC values were considered as significant when exceeding the average BC estimated from a set of random graphs (see Materials and Methods). In addition to DMN nodes, few nodes from other RSNs are slightly above significance. In contrast, nodes in different networks, including L/R pIPS (DAN), L/R SMA, and L CS (MOT), become more central than DMN nodes (L AG; pCC) (Fig. 2B and see [Supplementary Fig. 1D](#)) when the DMN is not strongly coupled (OUTSIDE-DMN epochs).

One possible confound is that the centrality of DMN nodes might be driven by connections within the DMN itself. This would artificially inflate the values of BC since the epochs were selected by the algorithm to have strong within-DMN coupling. To check for the influence of DMN internal connections on the BC values, the same analysis was run removing internal DMN

connections. While the absolute value of BC in DMN nodes (e.g., see pCC) is lower as expected, their centrality, compared with other regions of the brain, is relatively unaffected (see [Supplementary Fig. 2](#)).

To more systematically evaluate how node centrality varies depending on which network is internally coupled, we measured BC during each network's own period of strong coupling (INSIDE epochs for DAN, MOT, and VIS [used as a control]) (Fig. 3A). As before, significance was based on the average BC estimated from a set of random graphs (dashed line). We observed that different nodes become central depending on which network is internally coupled. However, specific nodes in DMN, DAN, and MOT maintain high BC values irrespective of which network is coupled. To better identify this group of central nodes, we considered both the mean (Fig. 3B left panel: red line) and consistency (defined as the percentage of times in which every node is above the random threshold, Fig. 3B left panel: bar plot) of BC values across all networks' INSIDE epochs. A few nodes, including L/R pIPS (DAN), pCC (DMN), and L SMA (MOT), remained both strongly central and consistent over time (Fig. 3B right panel: red bars).

In a final analysis, we examined the spatial structure of the graphs in relation to the centrality of the nodes identified above. Figure 4A shows graphs, obtained from Z-score matrices thresholded at the overall minimum ($Z = 2.5$) and maximum ($Z = 3.9$) values needed to maintain full connectedness, which were estimated during epochs of strong internal coupling for each network (INSIDE epochs, see above). It is evident that the spatial structure of the brain graph is quite different depending on which network is internally coupled (compare rows in Fig. 4A). At the low threshold ($Z = 2.5$), the brain is more densely connected during INSIDE epochs for DMN than for DAN, MOT, and VIS, respectively. At the high threshold ($Z = 3.9$), the graph remains fully connected during INSIDE-DMN epochs, with pCC being the most central node. The graph is less connected during DAN, MOT, and least during VIS INSIDE epochs. However, central nodes in the DAN (L/R pIPS) and MOT (SMA) maintain long-range connections with other nodes of the same or different networks. For instance, L pIPS is significantly connected with L FEF and R pIPS, part of the DAN, but also with L CS and SMA, part of the MOT network. In contrast, visual nodes (e.g., L/R V7) maintain predominantly local connections with other VIS nodes.

This impression was quantified by counting for each network at the highest threshold the number of internal, that is, within the same network, and external, that is, with nodes of other networks, connections (Fig. 5A, red/internal and black/external connections, respectively). To account for the different number of nodes considered for every RSN, we divided the total number of connections by the total number of possible internal ones. This analysis revealed that DMN, DAN, and MOT network centrality reflects a consistent number of external connections. In contrast, the centrality in of L/R V7 in the VIS network is local, mainly driven by internal connections.

Since BC values might be potentially affected by inter-nodal distance, we computed BC with edges of relative length obtained by weighting the functional coupling with the inter-nodal Euclidean Distance (ED) (Goni et al. 2014). In particular, to penalize pairs of nodes corresponding to short ED, we multiplied the functional z-scores by the $\log(\text{ED})$ as suggested in Lord et al. (2012) where a logarithmic trend was reported between these quantities. Furthermore, we adopted $\log(\text{ED})$ to mitigate the effect of extremely large values of ED which would otherwise mask out completely any contribution of the functional coupling. In Figure 5B, we report for the INSIDE-DMN epochs, the comparison between the BC obtained with weighted (red) and nonweighted (black)

edges. The correlation between the BC values for weighted and nonweighted edges was high ($r = 0.86$) indicating that the influence of distance is small.

In summary, these analyses confirm and extend our previous results (de Pasquale et al. 2012). First, we confirm that some nodes within the DMN, especially pCC, interact with many other regions outside DMN, when DMN is internally coupled. Second, we show that this rule applies to other networks since other nodes become central when their corresponding networks are internally coupled. However, specific nodes in different networks (pCC in the DMN, L pIPS in the DAN, L SMA in the MOT) occupy a central position irrespective of which RSN is internally coupled. These nodes are therefore candidate functional hubs for across-network interactions, because their centrality depends on a high number of external connections with other networks. In contrast, nodes of high centrality in the VIS network (e.g., L R V7) are more peripheral since their centrality reflects mainly internal connections, that is, within the VIS.

Global Efficiency and Integration

What is the function of these variations in network coupling topography and node centrality? One hypothesis is that these dynamics are important for functionally integrating different networks. To test this hypothesis, we investigated whether network dynamics correlate with the efficiency of the whole brain graph as measured by GE (see Materials and Methods). Figure 4B shows GE INSIDE (solid line) and OUTSIDE (dashed line) epochs for each network as a function of the threshold of the graph. For all RSNs, we found that the efficiency is higher when the network is strongly coupled (INSIDE, solid line) compared with when is not (OUTSIDE, dotted line), and this result generalizes across a range of graph thresholds (Fig. 4B). Interestingly, the range of estimated thresholds (yellow area) is greatest for DMN followed by DAN, MOT, and VIS. More importantly, the efficiency gap (OUTSIDE-INSIDE), that is, the average efficiency difference computed in the threshold range, is statistically significant and strongest in the DMN ($P < 10^{-5}$) followed by DAN ($P < 10^{-3}$), MOT ($P < 10^{-3}$), and VIS network ($P < 10^{-3}$). In summary, this result indicates that GE is higher when networks are coupled, and it is stronger during DMN coupling followed by DAN, MOT, and least during VIS coupling.

Temporal Dynamics of Efficiency and Network Coupling

The results presented thus far refer to properties averaged over time, that is, graph measures computed on a single adjacency matrix based on Z-scores averaged across specific temporal epochs (e.g., INSIDE or OUTSIDE-RSN epochs). However, we know that network coupling is nonstationary, which can in turn affect both centrality and efficiency. Therefore, a strategy was developed to study variations of BC and GE in time (see Materials and Methods for details) and relate those temporal fluctuations to RSN coupling. To define significant connections, a threshold was applied to the cross-correlation matrices based on a value that maximizes the overall BC of the graph (Fig. 6). To identify this value, we averaged across time the node BC estimated at every time point of every run of every subject as a function of the threshold ranging between [0 1]. We obtained a general BC increase in the range of cross-correlation $r \in [0.55; 0.65]$ with a maximum at $r = 0.6$ (red bars, Fig. 6 [bottom]). In this range of values (white dots), pCC, L SMA, and L/R pIPS showed the highest BC values when averaging across thresholds (Fig. 6 right panel, red bars). In these nodes, BC values were 3 standard deviations above the mean of BC values computed over the same thresholds

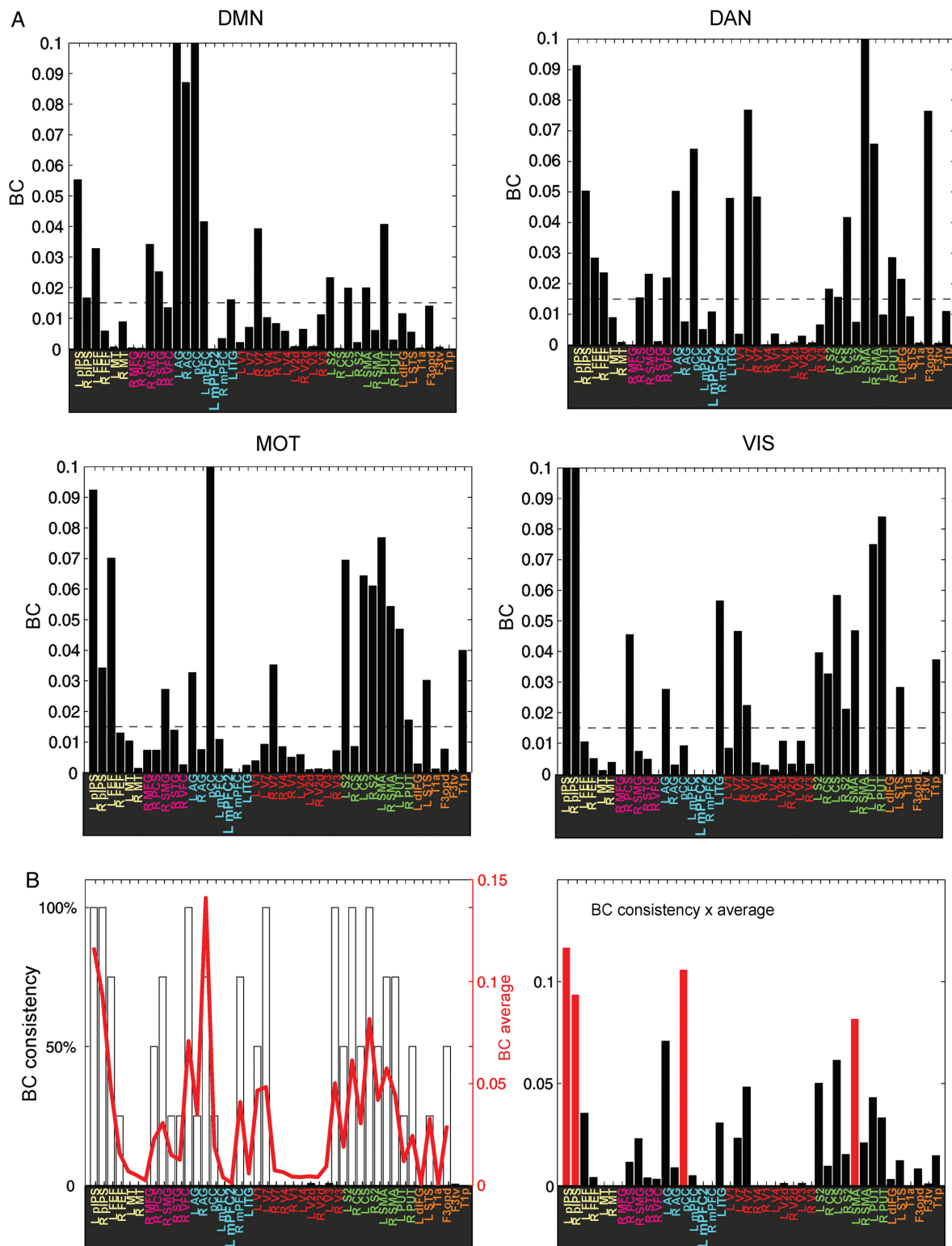


Figure 3. Network centrality. (A) BC for all the nodes during specific INSIDE epochs for DMN, DAN, MOT, and VIS networks. The nodes L/R pIPS, pCC, L SMA, and L V7 seem to be consistently central when their network is strongly coupled, but also during coupling of other networks. BC values are compared with the average BC from a set of equivalent random graphs (dashed line). (B) Left panel: The consistency of BC values above the random BC threshold (bars) and the BC value averaged across all RSN INSIDE epochs (red line). Right panel: the product (consistency) \times (average BC) identifies 3 main hubs: L/R pIPS, pCC, and L SMA.

across all nodes. This finding is consistent with the results based on average BC (Figs 2 and 3). Now, to relate node centrality to fluctuations of GE, based on the results in Figure 6, we adopted the

value $r = 0.6$ to obtain a temporal sequence of adjacency matrices for the dynamic graph analyses. Then, from this temporal sequence, we estimated a time course of GE for every run (bold

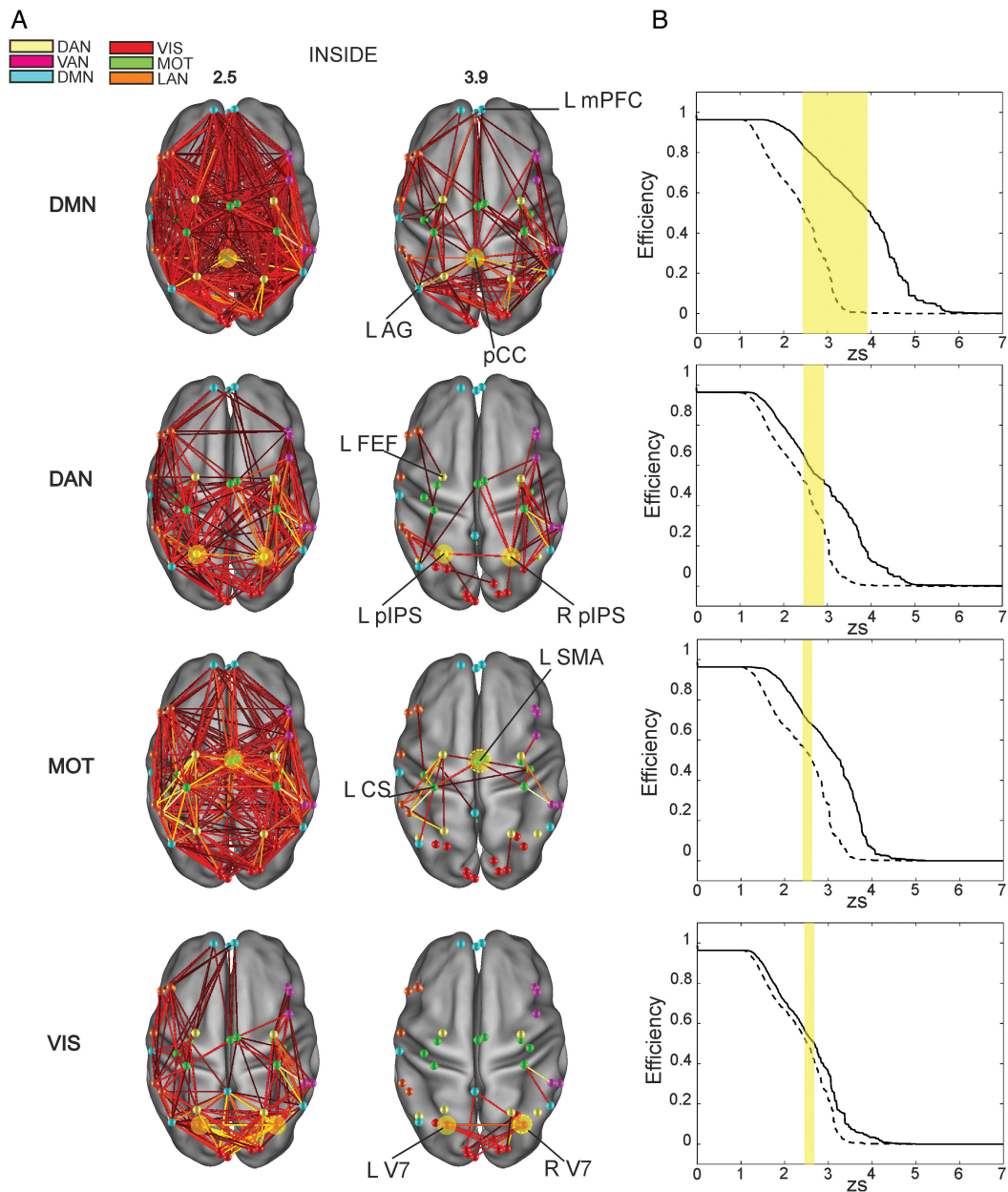


Figure 4. Network topology and global efficiency. (A) Graph structure of the candidate central networks computed in their specific INSIDE epochs corresponding to the highest ($z = 3.9$) and smallest ($z = 2.5$) thresholds, all RSNs. (B) Graph global efficiency (GE) computed INSIDE (solid line) and OUTSIDE (dashed line) each RSN epochs. The range of the thresholds (OUTSIDE-INSIDE) estimated for each RSN is highlighted in yellow.

line Fig. 7A). The GE time course shows fluctuations over time and on average GE is above its mean 49% of the total observed time showing a large amount of time in which the graph is efficiently integrated.

Next, we investigated the relationship between GE fluctuations and the occurrence of RSNs, that is, epochs of strong internal network coupling, with the hypothesis that epochs of high efficiency corresponded to periods of strong network coupling. The GE time course was thresholded above the mean (dotted line in Fig. 7A) for each run and binarized (see Materials and Methods). In what follows, for simplicity, we will define periods above the mean value as “efficiency peaks.” Similarly to GE, epochs of strong network coupling (INSIDE-RSN) were marked, and a second binarized time course was generated (Fig. 7A, rectangles). Next, to compare the binarized time series of GE and

RSN occurrence, we treated every network as a classifier of periods of high GE. Thus, we computed the TPR and FPR based on the percentage of temporal overlap between the 2 binarized time courses for every considered run (gray filled rectangles in Fig. 7A, see Material and Methods for details). Based on the estimated TPR and FPR for each network, an ROC (1 dot for every run) was computed, and the corresponding nonlinear fit (solid line) of TPR was plotted when all the central RSNs (DMN, DAN, and MOT) are considered separately (Fig. 7B) or together (see Fig. 8). When the overall contribution of the networks was considered, we obtained a good performance corresponding to a $d' = 0.6$ (see the corresponding ROC in Fig. 8). Furthermore, also when considered separately, DMN, DAN, and MOT exhibit good performance with a curve systematically above the chance level (Fig. 7B). When considering the concave curve fitting the TPR of the DMN, DAN, and

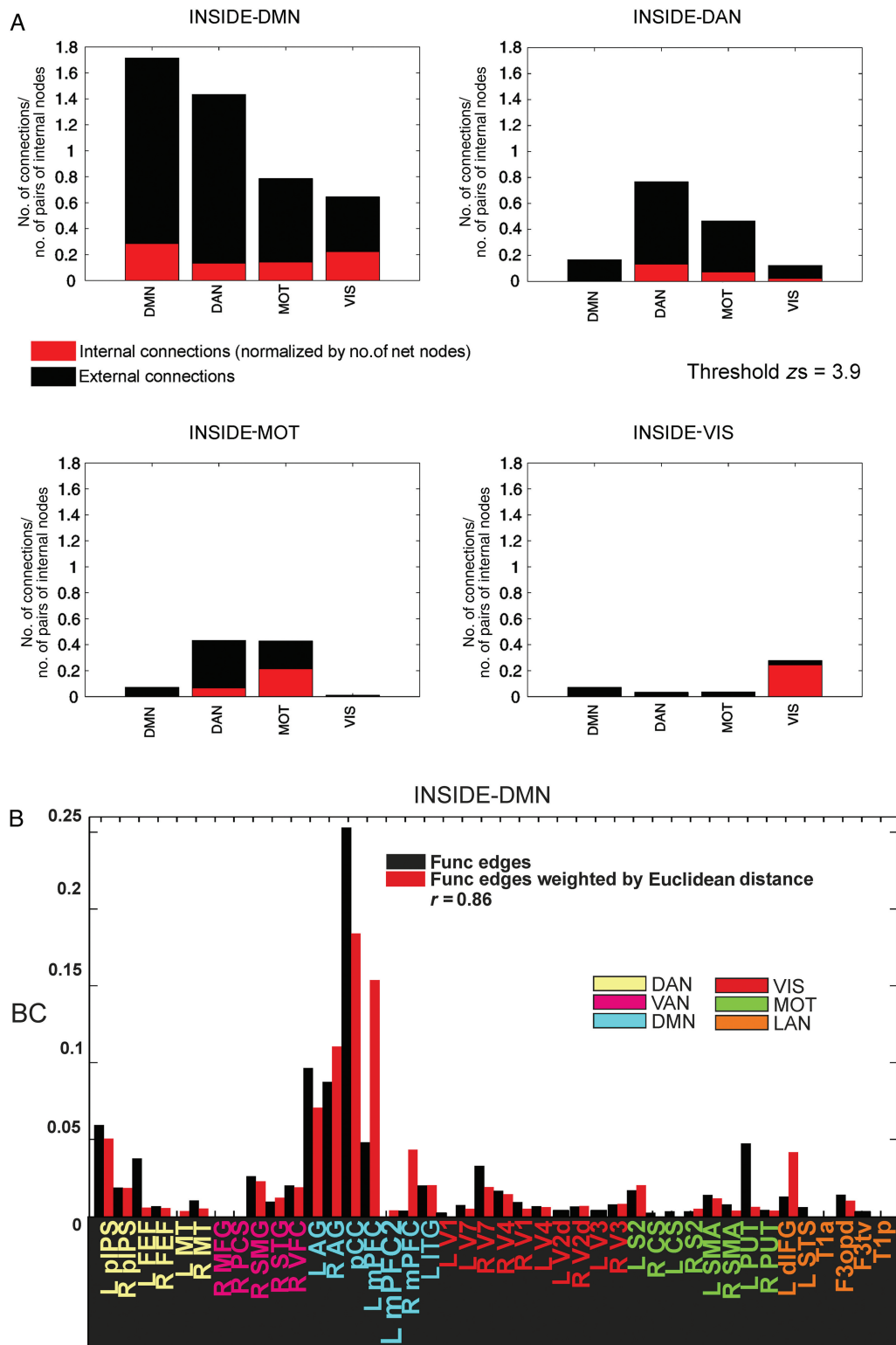


Figure 5. Internal versus external connections during network coupling. (A) The total number of internal (red) versus external connections (black) is shown at the highest threshold 3.9. To account for the different number of RSN nodes considered, both internal and external connections have been normalized by the number of all possible pairs of internal nodes for every network. (B) Comparison between BC obtained with edges weighted (red) and nonweighted by the Euclidean distance (black). We note a good agreement as proved by the high correlation between the 2 patterns, $r = 0.86$.

MOT epochs, the corresponding areas above the straight line were 48, 58, and 30%, corresponding to d' values of 0.32, 0.37, and 0.19, respectively. In contrast, VIS epochs did not perform better than a

random classifier (ROC reported, Fig. 7D). When the classification is based on coupling in any of the 3 central networks, we also obtained a good performance corresponding to a $d' = 0.6$

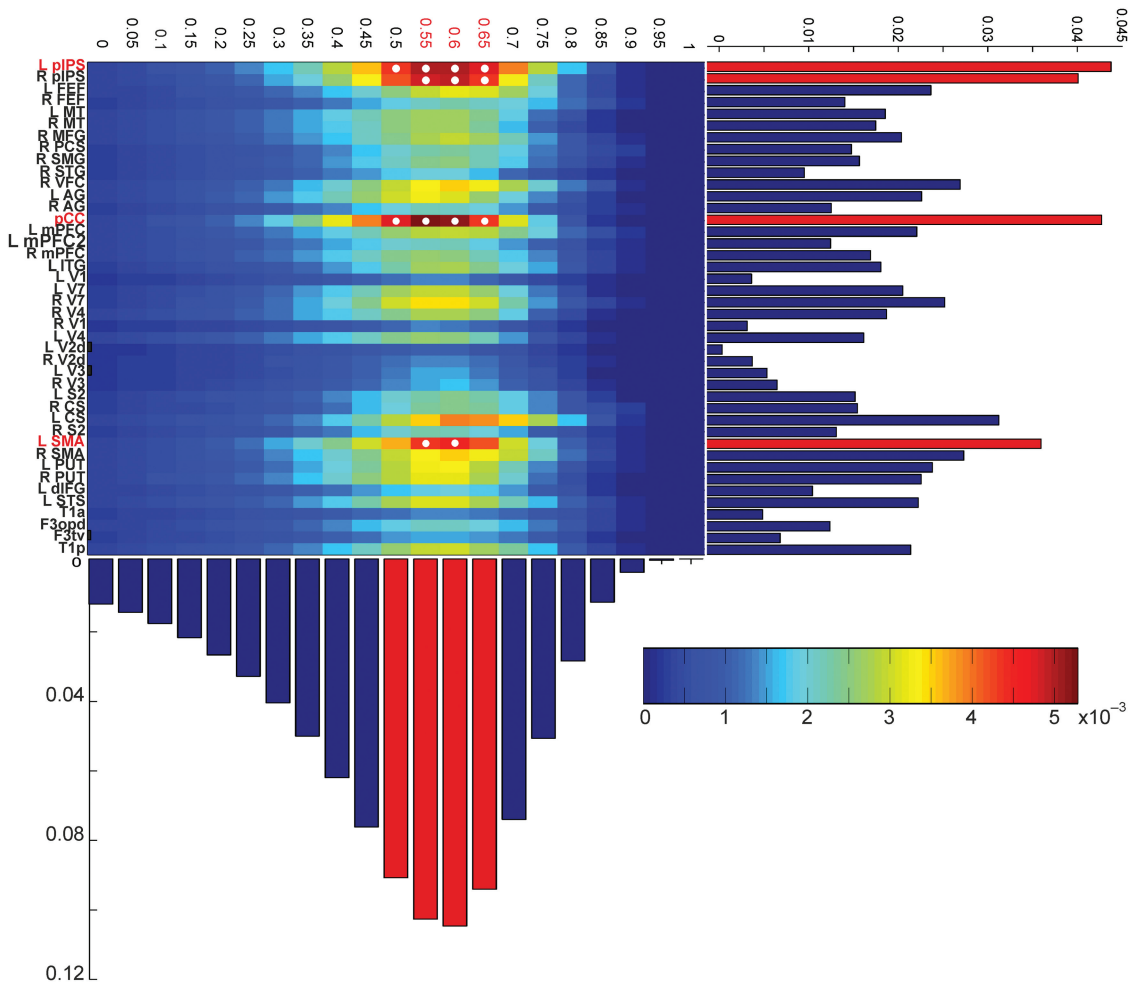


Figure 6. Betweenness centrality and hubs. The BC as a function of threshold: this matrix is obtained by averaging across time the BC computed at every time point of every run of every subject. We note 3 peaks corresponding to L/R pIPS, pCC, and L SMA corresponding to values higher than the mean + 3SDs (white dots). These nodes are consistently central when BC is averaged across thresholds (bar plot—right panel). The threshold range [0.55 0.65] corresponds to higher BC (bar plot—bottom panel).

(see the corresponding ROC in Fig. 8). This is evident from the confidence intervals of the estimated fitting parameters showing that the fitted curve was not statistically different from the bisecting line representing the chance level. The estimated parameters of the fit are reported in Table 2.

Overall, these findings indicate that the occurrence of RSN, that is, moments in which the correlation among the nodes of a network is strong, significantly predicts periods of high efficiency. However, since GE is a global and average measure of efficiency, a similar result could be obtained through different integration topologies: for instance, a graph with segregated communities linked by hubs or a fully connected but diffusely integrated (i.e., nonsegregated) graph. To gain more insight into the nature of changes in efficiency, we computed the time course of graph modularity, a measure related to network segregation (see Materials and Methods). We found that modularity was strongly anti-correlated with GE ($r = -0.82$, when averaged across runs), see Figure 7C where we report the correlation between these 2 time series computed in each session. This control is consistent with the idea that GE peaks are indexing true global integration across multiple networks.

An additional control was performed to test that the observed temporal overlap between RSN occurrence (e.g., DMN) and periods of high efficiency did not result from a spurious overlap of

2 random time series. To rule this out, we systematically shifted the 2 time courses at different time lags, in the range $[-60, 60]$ s, to check whether the agreement between efficiency and RSN occurrence was truly time-locked. A peak corresponding to lag 0 was observed which was statistically different from the baseline, that is, greater than $\mu_{\text{tail}} + 3\sigma_{\text{tail}}$ in which μ_{tail} and σ_{tail} are, respectively, the mean and standard deviation of TPR computed in the range $60 > |\text{lag}| > 20$ (see Supplementary Fig. 4). Analogous results were obtained for the other networks (not shown).

A final analysis considered the amount of total time occupied by the efficiency peaks that overlapped with the INSIDE epochs for DMN, DAN, and MOT. Since these networks show some temporal overlap (de Pasquale et al. 2010, 2012), we first considered the contribution of the epochs involving the DMN and then incrementally added the contribution of the epochs involving DAN and MOT. Importantly, each epoch was considered only once. We obtained that 71% of the efficiency peaks were explained by the cumulative contributions of DMN-, DAN-, and MOT-INSIDE epochs, and only 29% of the efficiency peaks remained unexplained (Fig. 7E).

In conclusion, these findings demonstrate that GE fluctuates over time in the resting state, and peaks of efficiency correspond to periods of strong network coupling for DMN, DAN, and MOT, but not for the VIS network. Thus, these RSNs not only predict

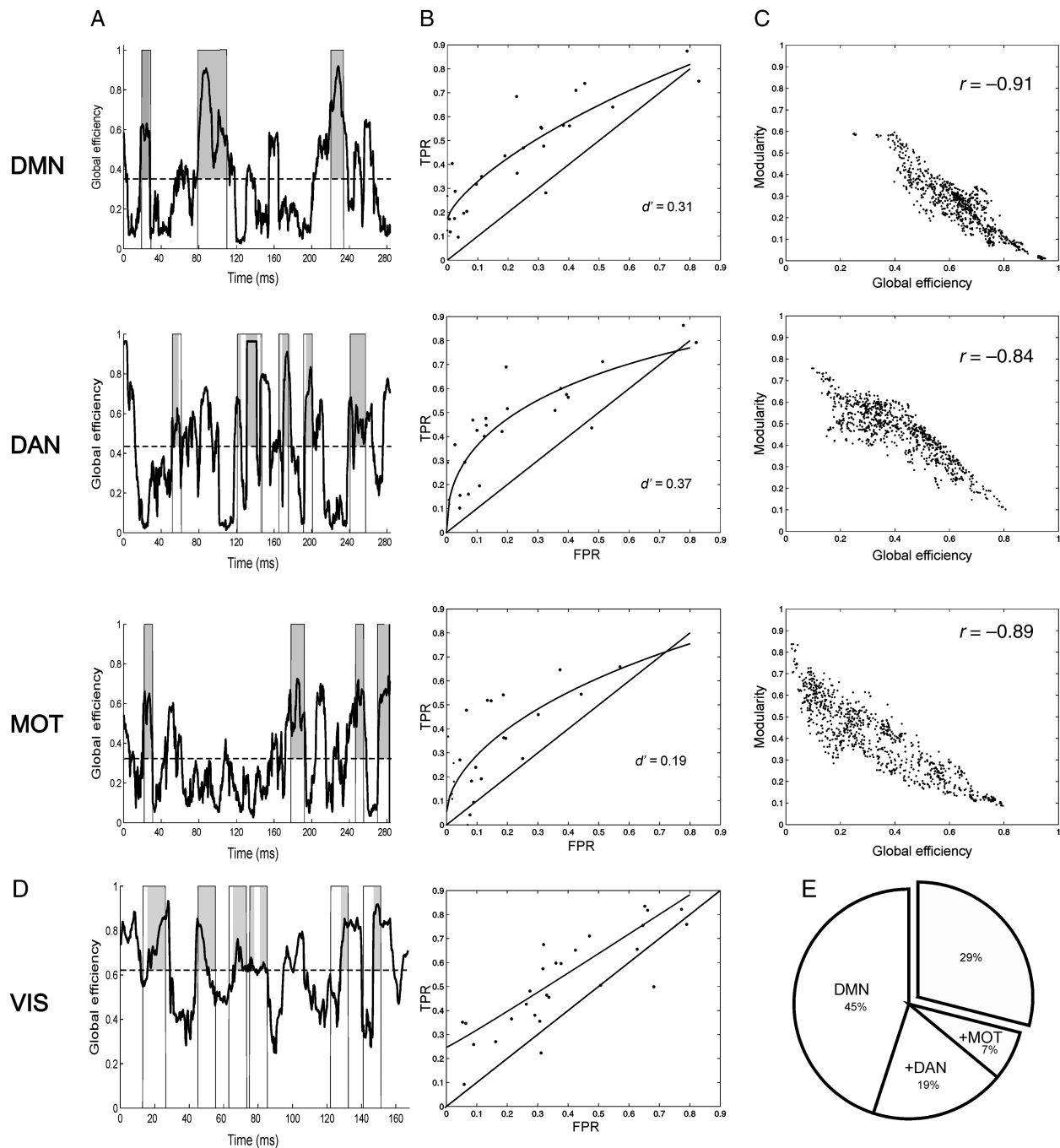


Figure 7. Temporal variability of global efficiency and network coupling. (A) GE time courses during representative runs. The global efficiency fluctuates over time (bold line) and presents peaks above the average value (dashed line). The temporal occurrence of INSIDE epochs for every network is reported in gray. The occurrence of RSNS seems to correspond to peaks of efficiency. (B) ROCs show good performance of DMN, DAN, and MOT as classifiers of efficiency peaks. (C) Correlation between the time series of efficiency and modularity computed in each considered session indicates a “true” global integration. (D) GE time courses and occurrence for the VIS network and corresponding ROC. (E) Percentage of global efficiency peaks covered by the incremental contributions of DMN (45%), DAN (19%), and MOT (7%). The temporal epochs of network coupling (RSNs) cover 71% of efficiency peaks.

the occurrence of efficiency peaks but also account for large fractions of efficiency peak variability.

Control for Nonstationarity of Connections

In previous work, we have reported evidence of a nonstationary coupling among RSN nodes (de Pasquale et al. 2010, 2012).

However, a formal and quantitative claim of nonstationarity requires an appropriate null hypothesis statistical testing. To this aim, we implemented the methodology proposed in Chang and Glover (2010) and Zalesky et al. (2014). Given its computational burden, we present a case study on 1 representative run in 1 representative subject. First, we estimated the order of a VAR model for fitting our BLP data from each of the 42 nodes using

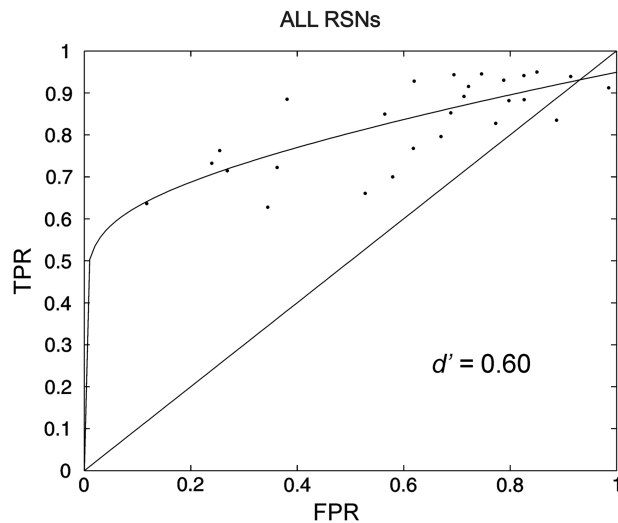


Figure 8. Network coupling as a classifier of efficiency peaks. ROC curve obtained when DMN, DAN, and MOT are considered jointly. These RSNs behave as good classifier leading to a $d' = 0.60$.

Table 2 Confidence intervals of the estimated parameters from the nonlinear fit of TPR, see equation (6)

$y = x^a - e^{-bx}/e^{-b} + c$	a	b	c
DMN	[0.445, 0.742]	[-0.417, -0.093]	[0.765, 1.024]
DAN	[0.240, 0.609]	[-0.505, -0.029]	[0.631, 0.931]
MOT	[0.380, 0.734]	[-0.675, 0.165]	[0.449, 1.124]
VIS	[0.281, 1.432]	[-0.552, 0.019]	[0.693, 1.174]

Only for the VIS network the estimated parameters are not statistically different from $[1, 0, 1]$ corresponding to the bisecting line. Thus, the performance of this network is not above the chance level.

the BIC letting the model order vary in the range $[1, 500]$. For each node and model order, we computed BIC and averaged it across all nodes. As shown in [Supplementary Figure 3A](#), the average BIC showed a minimum corresponding to 59 for the model order. Interestingly, given the temporal sampling of BLP is 20 ms, the estimated model order leads to a lag of approximately 10 s that is somehow in good agreement with the value of 8 s reported in [Zalesky et al. \(2014\)](#) estimated on fMRI data. [Supplementary Figure 3B](#) shows a comparison between the real (black) and the fitted (red) BLP for a representative run. In general, there was a good agreement between modeled and empirical BLP time series. Next, we proceeded to produce surrogate statistics from these modeled data [following [Chang and Glover \(2010\)](#)] to produce surrogate BLP data. We selected the nodes belonging to the proposed functional cores in each network: pCC (DMN), L SMA (MOT), L/R pIPS, and 1 node for each of the remaining RSNs, namely L STS (LAN), R-MFG (VAN), and R-V7 (VIS). For these nodes, we formally tested the nonstationarity of their connections by comparing it with 1000 surrogates of BLP time series as described in [Chang and Glover \(2010\)](#). For each surrogate connection, we computed the statistics proposed in [Zalesky et al. \(2014\)](#) to obtain a null distribution based on the sample of the 1000 realizations. From this distribution, we estimated the 95th percentile thus obtaining for each connection a threshold for nonstationarity. Finally, we computed the same statistics on the real data and compared, for each connection, the obtained values to the corresponding bootstrapped thresholds. Each

connection exceeding the threshold can be considered as statistically nonstationary. [Supplementary Figure 3C](#) shows statistically significant nonstationary connections (white blocks). Interestingly, candidate core nodes show more nonstationary connections than noncore nodes. For instance, across all connections (within and across network), pCC shows 47% of all connections as nonstationary, L SMA 40%, and L pIPS 36% (bar plot, see [Supplementary Fig. 3C](#)). In contrast, noncore nodes R MFG, L STS, and R V7 show fewer nonstationary connections. This result validates the previous observation that more “peripheral” networks VAN, VIS, and LAN, to which the latter nodes belong, respectively, spend more time in a state of internal coupling, whereas more “central” DMN, DAN, and MOT, to which the core nodes belong, show more cross-network interactions over time. In summary, these results support the evidence of a significant number of nonstationary connections for all candidate core nodes.

Discussion

This study presents 2 novel findings on the fundamental issue of how different brain regions or networks interact in the resting state. First, we demonstrate the existence of multiple dynamic hubs that allow for across-network coupling. In particular, specific nodes of the Default Mode, Dorsal Attention, and Motor networks behave as dynamical, that is, acting at distinct times, connectivity hubs of the brain. Second, dynamic network coupling and related variations in centrality correspond to increased global efficiency. Periods of strong within-network correlation correspond to periods of high efficiency, and 71% of these periods can be explained by the incremental contribution of these 3 networks. This suggests that the dynamic organization of cross-network interactions represents a property of the brain to optimize the efficiency in linking regions belonging to distinct functional domains. These results support the hypothesis of a dynamic core network model in which the core is composed of a set of network hubs alternating over time to ensure an efficient global communication in the whole brain.

Methodological Considerations

Graph Measures

A growing number of studies have applied graph theory to brain connectivity [reviewed in [Bassett et al. \(2013\)](#)], and some of these results are controversial, in part because of different definitions and strategies for estimation of the employed graph measures [see [Zuo et al. \(2012\)](#); [Power et al. \(2013\)](#) for an interesting discussion]. The interpretation of our results also depends on the adopted graph measures and several methodological choices that we made.

Our connectivity estimates do not contain any information on the coupling directionality and thus all the adopted measures are based on undirected graphs. Furthermore, we adopted binary graph measures based on thresholded interaction matrices to avoid the bias due to an eventual large number of edges with small weights.

To characterize local properties of the network and assess the potential impact of nodes on the network dynamics, we adopted the measure of node BC, designed to index patterns of information flow in brain networks and often found to covary with other measures of nodal centrality ([Zuo et al. 2012](#)). BC is high when a node participates in many of the network’s shortest paths, that is, when it acts as a “bridge” along pathways of strongest coupling ([Sporns 2011](#)). It is important to note that such a definition is very different from a measure based on degree in

which only the number of connections is taken into account. Thus, BC is less sensitive to the eventual inflation induced by the community size, see [Power et al. \(2013\)](#).

To characterize global network integration, we adopted the GE ([Sporns 2011](#)), a measure based on the definition of path length. In our case, we can interpret this efficiency as the ability of the brain as a system to effectively communicate across its components. It is important to stress that due to the average or global nature of the measure, it is not possible to distinguish a network with segregated communities that are linked by hubs or a fully connected but diffusely integrated (i.e., nonsegregated) network. To gain better insight into which topological features were associated with high or low efficiency, we computed the graph modularity, a quantity used to identify segregated communities in the graph. Our results demonstrated that efficiency and modularity were significantly anti-correlated, thus confirming that periods of high efficiency were associated with functional integration of network communities.

It is important to note that efficiency and modularity strongly depend on the connection density of the graph. In particular, when we analyzed the dynamics of BC, efficiency, and modularity, we adopted a common threshold for the connectivity matrices. This choice led to a sequence of adjacency matrices whose connection density is not fixed. Although we acknowledge that the different sparseness of these matrices might be problematic and influence estimates of the graph measures, we believe that this issue did not impact the validity of our findings for several reasons. Firstly, it is not possible to compare the dynamics of network integration and RSN occurrence (as labeled through the EMCW algorithm) by fixing the connection density. This would lead to a sequence of adjacency matrices thresholded at different connectivity amplitudes while the EMCW strategy identifies patterns of strong connectivity amplitude. Notably, the obtained relationship between RSN occurrence and efficiency/density is not trivial, that is, it is not given that periods in which networks are highly coupled correspond to strong integration, characterized by a higher density of connections and efficiency. This is because the number of nodes internal to an RSN is only approximately 15% of the total number of nodes considered. Thus, in epochs in which a RSN is strongly internally coupled, the number of internal connections should not inflate the overall density. An important control on this point is that the VIS network, which has the highest number of nodes (VIS 10 nodes; DMN 6 nodes), did not show a significant relationship between GE peaks and RSN occurrence.

Secondly, it is also unlikely that the connection density influenced the results on global integration and node centrality when comparing INSIDE- versus OUTSIDE-RSN epochs. In fact, we computed DMN efficiency and modularity as a function of graph density (see [Supplementary Fig. 5](#)). Interestingly, we note that at a density value of approximately 0.2, corresponding to a graph fully connected during OUTSIDE epochs, the efficiency is higher and the modularity is lower during INSIDE versus OUTSIDE epochs. Furthermore, the thresholds used on the z-score matrices estimated during INSIDE- versus OUTSIDE-DMN epochs led to similar values of the graph density. Specifically, the density of connections during INSIDE and OUTSIDE-DMN epochs was 0.15 and 0.17, respectively (see [Fig. 2](#)). With regard to other central networks (DAN and MOT), the graph densities were 0.22 and 0.26, respectively. This control shows that the thresholds applied to the Z-score matrices before computing centrality yield graph with similar densities during INSIDE versus OUTSIDE epochs. Therefore, we conclude that the influence of different graph densities on the BC results is minimal, at least for the thresholds we adopted.

Signal Leakage

Every MEG-based connectivity study can be seriously affected by “signal leakage” which is an extensive term for a number of separate effects among which spatial spread of sources and spatial misattribution of sources induced by an inaccurate forward field computation ([Brookes et al. 2012](#)). Basically, spurious connectivity can be observed due to the nonindependence of signals at separate brain locations. Such connectivity does not reflect a “true” coupling of the considered nodes but is merely due to the inaccuracy of the source-space projection.

Several techniques have been proposed to quantify, minimize, and account for this effect ([Nolte et al. 2004](#); [Brookes, Hale, et al. 2011](#); [Brookes et al. 2012](#); [Hipp et al. 2012](#); [Marzetti et al. 2013](#)). Most of these techniques are based on discarding zero lag interactions among MEG signals, assuming that this contribution is entirely due to the source leakage. While this approach is effective in correlation mediated by the field spread, it will also suppress genuine neurophysiological interactions that occur at zero lag ([Brookes et al. 2014](#)). From a biological perspective, estimates of connectivity among orthogonalized signals are likely different from those computed on nonorthogonalized signals as in the present work. In fact, a procedure in which only orthogonalized signals are maintained will highlight connections from sources that are maximally out of phase. Such connections represent an interesting aspect of the interaction framework, which is complementary to the one we would like to investigate here based on zero lag interactions. Moreover, the majority of the above techniques operate on the first main MEG signal component among the 3 available ones. This choice is somehow arbitrary since often at rest at least 2 components show similar amplitude. For this reason, in our approach, the BLP is computed maintaining all the 3 components of the signal.

In this work, to account for source leakage, we removed connections whose inter-nodal distance is <35 mm [see [de Pasquale et al. \(2010\)](#); [de Pasquale et al. \(2012\)](#) where these aspects are discussed]. However, we acknowledge that source leakage might still potentially have an effect on our results, and thus, we performed the following controls. First, source leakage can potentially lead to arbitrary and simultaneous increase of power in separate brain regions, which would inflate their coupling and cause a good correspondence between peaks of GE and RSN occurrence. To control for this effect, we compared the time courses of GE and mean BLP estimated in the central networks (DMN, DAN, and MOT). In particular, we computed the correlation between GE and BLP time series for each run and then averaged across runs. We obtained very low values of correlation (r), namely $r(\text{GE, BLP-DMN}) = 0.18$, $r(\text{GE, BLP-DAN}) = 0.19$, $r(\text{GE, BLP-MOT}) = 0.22$. As an example, we report in [Supplementary Figure 6](#) the scatterplot between these quantities for a representative run. This control indicates no significant relationship between increases of BLP and peaks of global efficiency; hence, our observations on the relationship between GE and RSN occurrence seem robust with respect to signal leakage.

Secondly, we note that nodes that are very close in distance often have different levels of centrality, for example, left and right SMA that are just juxtaposed on the medial wall of the frontal lobe have different levels of centrality (high in left, but low in right SMA). To generalize this observation, we examined systematically the relationship between Euclidean distance and BC. [Supplementary Figure 7](#) plots for every node the relationship between BC as computed in [Figure 3](#) and the average value of the Euclidean distance of the connections involved for each node in the computation of the centrality. Overall the correlation between these quantities was not statistically significant ($r = 0.19$,

$P = 0.21$). Furthermore, connections that include the dynamic hubs (underlined labels) do not correspond to the shortest possible connections, and connections from other 11 noncentral nodes fall in the very same range of distance as the most central ones (light gray). Finally, a large fraction of nodes (~30%) have short connections and low BC (dark gray-shaded area). In general, dynamic hubs realize their centrality by means of long-range connections, many of which external with respect to their network (see [Supplementary Figs 2 and 5B](#)).

In summary, our controls indicate that neither GE nor BC measures are influenced by signal leakage. Moreover, BC values do not seem to be affected by local connections, but rather depend on long-range connections.

Dynamic Cortical Hubs

In connectivity studies, every brain region can be potentially assigned a connectional fingerprint defining its structural or functional role ([Hutchison et al. 2013](#)). A key role in the mechanisms of integration flow in the brain is potentially played by cortical hubs consisting of highly connected areas serving as way stations for network traffic or as centers of integration ([Shirer et al. 2012](#)). Several structural and functional hub locations have been reported in multimodal imaging studies ([Hagmann et al. 2008](#); [Bullmore and Sporns 2012](#)) typically located in medial (pCC) and lateral (angular gyrus) parietal regions of the DMN, as well as in anterior cingulate and anterior insula, part of the cingulo-opercular (CO), and lateral frontal and parietal cortex, part of the frontoparietal control networks ([Buckner et al. 2009](#); [Cole et al. 2010](#); [Tomasi and Volkow 2011](#); [de Pasquale et al. 2012, 2013](#)) [see [Power et al. \(2013\)](#) for opposed results in which these DMN regions are assigned only a provincial role due to degree inflation caused by community size]. In line with these results, in a previous MEG study, we identified a set of nodes belonging to the DMN as highly central. Additional nodes from DAN and MOT networks were also found to be central, although with a lower connectivity strength ([de Pasquale et al. 2012](#)).

In this study, we investigated these aspects by using graph theory measures that allow for a more quantitative definition of centrality. When centrality amplitude and reproducibility measures were combined ([de Pasquale et al. 2013](#)), 3 nodes were identified: pCC in the DMN; L/R pIPS in the DAN; and left SMA in the MOT networks (Figs 3–6). These nodes behaved as hubs not just during temporal epochs in which the networks to which they belong were coupled, but also during epochs of other networks' engagement. Of note, the functional centrality of pCC and L SMA is in agreement with prior fMRI results ([Yeo et al. 2011](#); [de Pasquale et al. 2013](#)). It is intriguing to speculate that the location of these dynamical hubs allows for the integration of internal cognitive processes (e.g., memory, self-referential behavior) mediated by the DMN ([Buckner et al. 2008](#); [Sestieri et al. 2010](#)), with the selection of environmental and body information mediated by the DAN ([Sestieri et al. 2010](#); [Corbetta and Shulman 2002](#)), and for each system, in turn, linkage with response/sensory-motor programming and execution mediated by the MOT network. Thus, the integration among these systems may be necessary to provide a more complete coverage across a broad range of functional domains. Cycling through these patterns of dynamic activity occurs at rest consistent with the idea that resting-state activity partly recapitulates high-frequency patterns of task-evoked activation ([Fox et al. 2005](#); [Lewis et al. 2009](#); [Baldassarre et al. 2012](#)).

Dynamic analyses of graph properties and network coupling revealed a number of novel facts about RSNs. We showed that highly central nodes in different RSNs behave as transient

hubs, that is, they are central during different temporal epochs even though with some periods of overlap. This is illustrated in the movie reported in [Figure 9](#), in which one 20-s period from 1 representative run in 1 subject is analyzed. The upper left panel shows the temporal series of peaks of centrality for the identified hubs, (L/R pIPS, pCC, and L SMA) and their duration. The lower left panel reports the instantaneous values of BC (not-normalized) for individual nodes in DMN, DAN, and MOT networks. Finally, the right panel displays the graph connections. The hypothesized dynamic core is highlighted in red. The 3 panels are temporally synchronized. Inspection of the movie illustrates the alternation of different graph configurations that are centered on the 3 main hubs.

When averaged across runs, BC peaks for DMN occur 45% of time, for MOT 43% and for DAN 41%. The temporal interchange of these hubs is fundamental for allowing an efficient network integration in the brain, but at the same time is problematic since leads to the following paradox: if a network consists, by definition, of a set of nodes showing higher internal coupling than with the rest of the brain, how can these nodes also significantly interact with each other? An examination of temporal dynamics points to 1 possible answer. Given networks are nonstationary, as emerging findings suggest [[Hutchison et al. \(2013\)](#) for a review], epochs in which they are not highly coupled are exploited to integrate with other systems. Our results suggest that this is achieved through dynamic hubs and long-range connections. Now, since the putative hubs relate to important and distinct functions such as internal cognition, sensory-motor processing, and attention, we speculate that their alternation reflects fundamental axes of integration processing in the brain that are partially segregated at rest. An important prediction is that these dynamics should dramatically be altered during tasks that emphasize either internal or external cognition.

Global Efficiency and RSN Occurrence

The model of transient hubs that link separate functional domains in the brain suggested us a computational strategy for optimizing the global flow of interaction. To this aim, we investigated the dynamics of the graph global efficiency. Interestingly, but perhaps not surprisingly, we found that efficiency is not fixed but fluctuates over time (see [Fig. 7](#)) showing a large number of peaks, namely 49% of total observed time. Furthermore, this state of high efficiency correlates with the emergence of specific RSNs, namely DMN, DAN, and MOT (with the visual network representing a negative control). These networks behave as classifiers of efficiency peaks ([Figs 7 and 8](#)) and 70% of them could be explained by the incremental contribution of these RSNs. These results combined with the previous considerations on the node centrality suggest that the transient formation of hubs during periods of high internal coupling in some RSNs (DMN, DAN, and MOT) but not others (VIS) correspond to the optimization of the GE of the graph.

A “Dynamic Core Network” Model

Diverse theories of cognition and consciousness hypothesize the existence of distributed neural systems as a basis for a “global workspace,” a core system in which segregated functional communities interact ([Dehaene et al. 1998](#); [Dehaene and Naccache 2001](#)). A possible structural substrate of such global workspace may be found in rich club organization ([McAuley et al. 2007](#); [Bullmore and Sporns 2009](#)). This model predicts a spatially distributed and yet topologically central organization

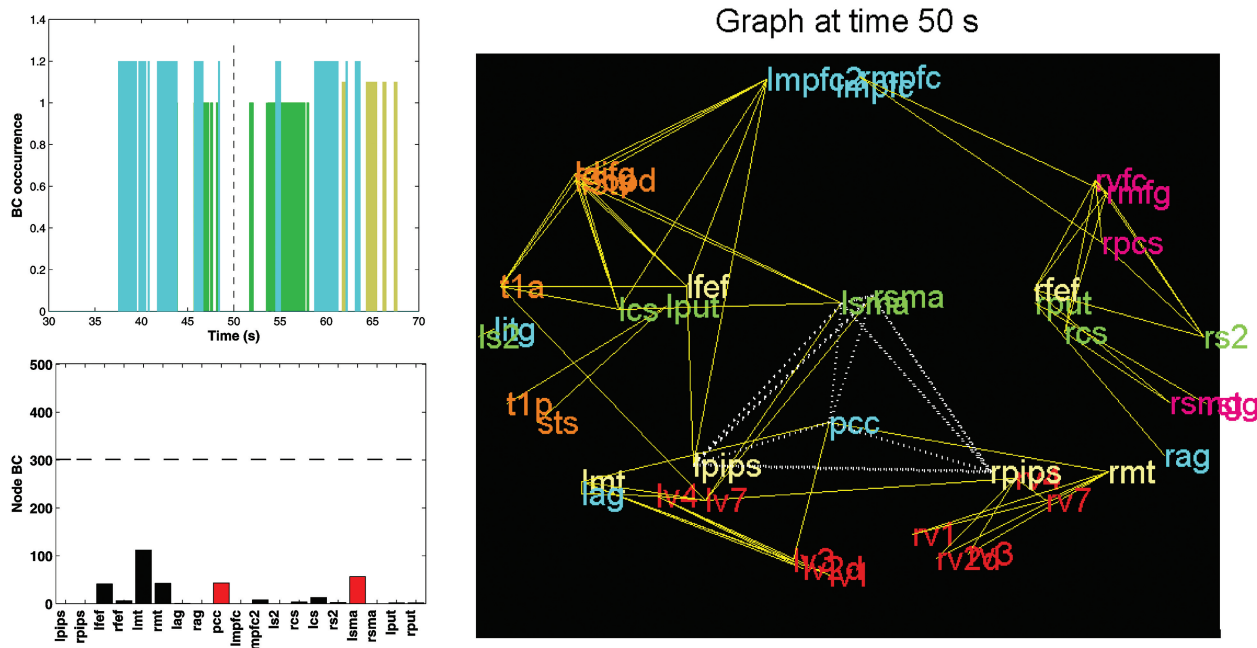


Figure 9. Movie of dynamic hubs and connectivity. A 20 s sample in 1 representative run (see attached movie). In the upper left panel, we show the dynamics of the occurrence of peaks of centrality for the identified dynamic hubs (L/R pIPS, pCC, and L SMA); in the lower left panel, we report the instantaneous values of BC (not normalized) for the nodes of DMN, DAN, and MOT at every time point, and in the right panel, we display the graph connections. The hypothesized dynamic core is highlighted in red. The 3 panels are temporally synchronized.

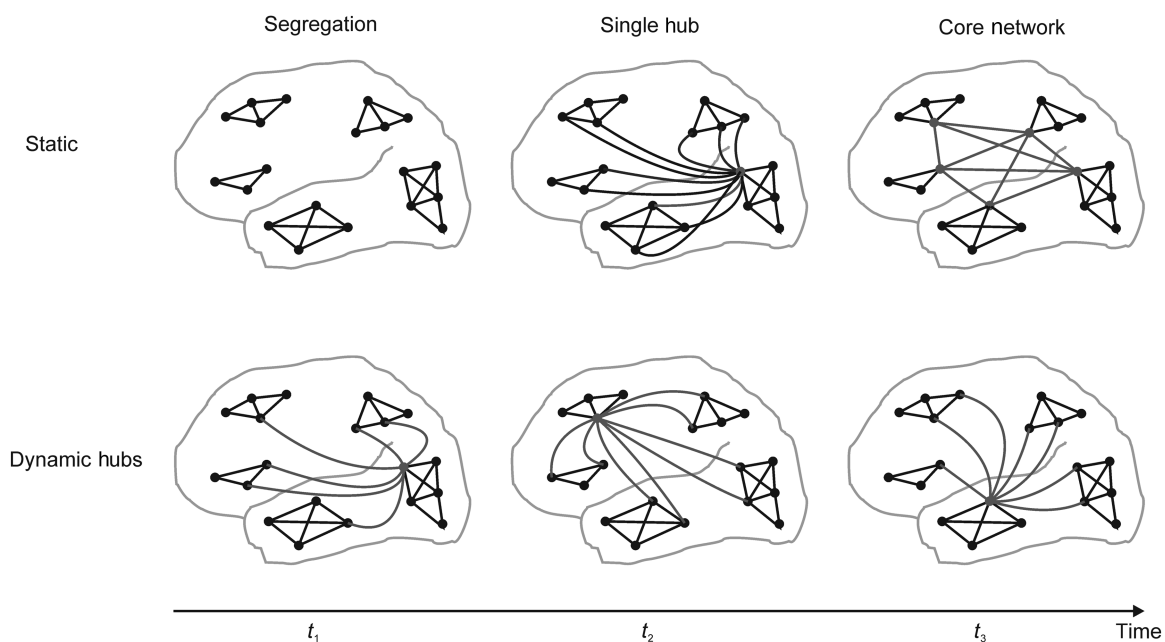


Figure 10. The dynamic core network model. Transient hubs belonging to specific RSNs at distinct time points ensure an efficient flow of integration across the whole brain.

in which hubs of a network tend to be densely interconnected. The presence, or absence, of such organization can provide important information on the higher order structure of a network, particularly at the level of resilience, hierarchal ordering, and specialization (McAuley et al. 2007). Interestingly, although no anatomical information was used in our analysis, the

nodes that we identified as dynamical hubs largely overlap with the areas reported in the study by van den Heuvel and Sporns (2013) as composing the rich club, and our results are consistent with findings demonstrating that the structural rich club cross-links functional RSNs (van den Heuvel and Sporns 2013).

Thus, we speculate that such a core structure could be interpreted as the anatomical substrate of our dynamic integration model that closely resembles the hypothesized “connective core” described in study by Shanahan (2012). In fact, many aspects of this model seem to fit our results. First, the fact that these hubs involve different functional domains might relate to the “coalition formation” problem, namely how the set of processes relevant to the ongoing situation becomes active and join a coalition. We speculate that this could be accomplished by exploiting the dynamic availability of the different hubs (see Fig. 10). Moreover, our dynamic core is versatile, that is, the temporal dynamics observed at rest could become more structured in the presence of a stimulus [as shown for example in study by Betti et al. (2013)]. Notably, our results provide a possible electrophysiological correlate of recent fMRI findings in which strong dynamic nonstationary and intermodular connections involving hubs of DMN and frontoparietal systems are reported (Zalesky et al. 2014). Interestingly, network fluctuations are linked to efficiency of information transfer, thus suggesting that the brain dynamics reflects a balance between efficient information-processing and metabolic expenditure. Furthermore, our observations are also in line with modeling predictions based on structural data (Honey et al. 2007) in which structure–function relations at multiple temporal scales are identified with the functional centrality of individual nodes varying across time as inter-regional couplings shift. In line with our findings, in this work it is suggested that the neuronal dynamics may lead to the existence of hubs in functional connectivity networks and functional clusters bridged via areas in primary somatosensory motor cortex (Honey et al. 2007).

Supplementary Material

Supplementary material can be found at <http://www.cercor.oxfordjournals.org/> online.

Funding

This work was supported by the European Community’s Seventh Framework Programme (FP7/2007–2013), Grant Agreement HEALTH-F2-2008-200728 “BrainSynch” NIH grant, and NIH grants 1R01MH096482 to M.C., and the Human Connectome Project (1U54MH091657-01) from the 16 National Institutes of Health Institutes and Centers that support the NIH Blueprint for Neuroscience Research.

Notes

We thank Catie Chang for providing us with the original code developed for the VAR model analyses. Furthermore, we thank Jaroslav Hlinka, Milan Palus, and David Hartman for fruitful discussions on graph measures. *Conflict of Interest:* None declared.

References

- Achard S, Bullmore E. 2007. Efficiency and cost of economical brain functional networks. *PLoS Comput Biol.* 3:e17.
- Baldassarre A, Lewis CM, Committeri G, Snyder AZ, Romani GL, Corbetta M. 2012. Individual variability in functional connectivity predicts performance of a perceptual task. *Proc Natl Acad Sci USA.* 109:3516–3521.
- Bassett DS, Wymbs NF, Rombach MP, Porter MA, Mucha PJ, Grafton ST. 2013. Task-based core-periphery organization of human brain dynamics. *PLoS Comput Biol.* 9:e1003171.
- Beckmann CF, DeLuca M, Devlin JT, Smith SM. 2005. Investigations into resting-state connectivity using independent component analysis. *Philos Trans R Soc Lond B Biol Sci.* 360:1001–1013.
- Betti V, Della Penna S, de Pasquale F, Mantini D, Marzetti L, Romani GL, Corbetta M. 2013. Natural scenes viewing alters the dynamics of functional connectivity in the human brain. *Neuron.* 79:782–797.
- Biswal BB, Van Kylen J, Hyde JS. 1997. Simultaneous assessment of flow and BOLD signals in resting-state functional connectivity maps. *NMR Biomed.* 10:165–170.
- Blondel VD, Guillaume JL, Lambiotte R, Lefebvre E. 2008. Fast unfolding of communities in large networks. *J Stat Mech Theory Expt.* 10:1008–1020.
- Brookes M, Woolrich M, Luckhoo H, Price D, Hale JR, Stephenson MC, Barnes GR, Smith SM, Morris PG. 2011. Investigating the electrophysiological basis of resting state networks using magnetoencephalography. *Proc Natl Acad Sci USA.* 108:16783–16788.
- Brookes MJ, Hale JR, Zumer JM, Stevenson CM, Francis ST, Barnes GR, Owen JP, Morris PG, Nagarajan SS. 2011. Measuring functional connectivity using MEG: methodology and comparison with fMRI. *Neuroimage.* 56:1082–1104.
- Brookes MJ, O’Neill GC, Hall EL, Woolrich MW, Baker A, Palazzo Corner S, Robson SE, Morris PG, Barnes GR. 2014. Measuring temporal, spectral and spatial changes in electrophysiological brain network connectivity. *Neuroimage.* 91: 282–299.
- Brookes MJ, Woolrich MW, Barnes GR. 2012. Measuring functional connectivity in MEG: a multivariate approach insensitive to linear source leakage. *Neuroimage.* 63:910–920.
- Buckner RL, Andrews-Hanna JR, Schacter DL. 2008. The brain’s default network: anatomy, function, and relevance to disease. *Ann NY Acad Sci.* 1124:1–38.
- Buckner RL, Sepulcre J, Talukdar T, Krienen FM, Liu H, Hedden T, Andrews-Hanna JR, Sperling RA, Johnson KA. 2009. Cortical hubs revealed by intrinsic functional connectivity: mapping, assessment of stability, and relation to Alzheimer’s disease. *J Neurosci.* 29:1860–1873.
- Bullmore E, Sporns O. 2009. Complex brain networks: graph theoretical analysis of structural and functional systems. *Nat Rev Neurosci.* 10:186–198.
- Bullmore E, Sporns O. 2012. The economy of brain network organization. *Nat Rev Neurosci.* 13:336–349.
- Chang C, Glover GH. 2010. Time-frequency dynamics of resting-state brain connectivity measured with fMRI. *Neuroimage.* 50:81–98.
- Cole MW, Bassett DS, Power JD, Braver TS, Petersen SE. 2014. Intrinsic and task-evoked network architectures of the human brain. *Neuron.* 83:238–251.
- Cole MW, Pathak S, Schneider W. 2010. Identifying the brain’s most globally connected regions. *Neuroimage.* 49: 3132–3148.
- Corbetta M, Shulman GL. 2002. Control of goal-directed and stimulus-driven attention in the brain. *Nat Rev Neurosci.* 3:201–215.
- Dai D, Huiguang H. 2011. VisualConnectome: Toolbox for brain network visualization and analysis Abstract-Human Brain Mapping. <http://code.google.com/p/visualconnectome/>.
- Damoiseaux JS, Rombouts SA, Barkhof F, Scheltens P, Stam CJ, Smith SM, Beckmann CF. 2006. Consistent resting-state

- networks across healthy subjects. *Proc Natl Acad Sci USA*. 103:13848–13853.
- de Pasquale F, Barone P, Sebastiani G, Stander J. 2004. Bayesian analysis of dynamic magnetic resonance breast images. *Appl Statist*. 53:18.
- de Pasquale F, Della Penna S, Snyder AZ, Lewis C, Mantini D, Marzetti L, Belardinelli P, Ciancetta L, Pizzella V, Romani GL, et al. 2010. Temporal dynamics of spontaneous MEG activity in brain networks. *Proc Natl Acad Sci USA*. 107:6040–6045.
- de Pasquale F, Della Penna S, Snyder AZ, Marzetti L, Pizzella V, Romani GL, Corbetta M. 2012. A cortical core for dynamic integration of functional networks in the resting human brain. *Neuron*. 74:753–764.
- de Pasquale F, Sabatini U, Della Penna S, Sestieri C, Caravasso C, Formisano R, Peran P. 2013. The connectivity of functional cores reveals different degrees of segregation and integration in the brain at rest. *Neuroimage*. 69:51–61.
- Dehaene S, Kerszberg M, Changeux JP. 1998. A neuronal model of a global workspace in effortful cognitive tasks. *Proc Natl Acad Sci USA*. 95:14529–14534.
- Dehaene S, Naccache L. 2001. Towards a cognitive neuroscience of consciousness: basic evidence and a workspace framework. *Cognition*. 79:1–37.
- Della Penna S, Del Gratta C, Granata C, Pasquarelli A, Pizzella V, Rossi R, Russo M, Torquati K, Ernè S. 2000. Biomagnetic systems for clinical use. *Philos Mag B*. 80:937–948.
- Dosenbach NU, Fair DA, Miezin FM, Cohen AL, Wenger KK, Dosenbach RA, Fox MD, Snyder AZ, Vincent JL, Raichle ME, et al. 2007. Distinct brain networks for adaptive and stable task control in humans. *Proc Natl Acad Sci USA*. 104:11073–11078.
- Doucet G, Naveau M, Petit L, Delcroix N, Zago L, Crivello F, Jobard G, Tzourio-Mazoyer N, Mazoyer B, Mellet E, et al. 2011. Brain activity at rest: a multiscale hierarchical functional organization. *J Neurophysiol*. 105:2753–2763.
- Engel AK, Gerloff C, Hilgetag CC, Nolte G. 2013. Intrinsic coupling modes: multiscale interactions in ongoing brain activity. *Neuron*. 80:867–886.
- Fox MD, Snyder AZ, Vincent JL, Corbetta M, Van Essen DC, Raichle ME. 2005. The human brain is intrinsically organized into dynamic, anticorrelated functional networks. *Proc Natl Acad Sci USA*. 102:9673–9678.
- Friston K. 2002. Beyond phrenology: what can neuroimaging tell us about distributed circuitry? *Annu Rev Neurosci*. 25:221–250.
- Goni J, van den Heuvel MP, Avena-Koenigsberger A, Velez de Mendizabal N, Betzel RF, Griffa A, Hagmann P, Corominas-Murtra B, Thiran JP, Sporns O. 2014. Resting-brain functional connectivity predicted by analytic measures of network communication. *Proc Natl Acad Sci USA*. 111:833–838.
- Hacker CD, Laumann TO, Szrama NP, Baldassarre A, Snyder AZ, Leuthardt EC, Corbetta M. 2013. Resting state network estimation in individual subjects. *Neuroimage*. 82:616–633.
- Hagmann P, Cammoun L, Gigandet X, Meuli R, Honey CJ, Wedeen VJ, Sporns O. 2008. Mapping the structural core of human cerebral cortex. *PLoS Biol*. 6:e159.
- He BJ, Snyder AZ, Zempel JM, Smyth MD, Raichle ME. 2008. Electrophysiological correlates of the brain's intrinsic large-scale functional architecture. *Proc Natl Acad Sci USA*. 105:16039–16044.
- Hipp JF, Hawellek DJ, Corbetta M, Siegel M, Engel AK. 2012. Large-scale cortical correlation structure of spontaneous oscillatory activity. *Nat Neurosci*. 15:884–890.
- Honey CJ, Kotter R, Breakspear M, Sporns O. 2007. Network structure of cerebral cortex shapes functional connectivity on multiple time scales. *Proc Natl Acad Sci USA*. 104:10240–10245.
- Honey CJ, Sporns O, Cammoun L, Gigandet X, Thiran JP, Meuli R, Hagmann P. 2009. Predicting human resting-state functional connectivity from structural connectivity. *Proc Natl Acad Sci USA*. 106:2035–2040.
- Hu TC, Kahng AB, Tsao CA. 1995. Old bachelor acceptance: a new class of non-monotone threshold accepting methods. *ORSA J Comput*. 7:417–425.
- Hutchison R, Womelsdorf T, Allen E, Bandettini P, Calhoun V, Corbetta M, Della Penna S, Duyn J, Glover G, Gonzalez-Castillo J, et al. 2013. Dynamic functional connectivity: promise, issues, and interpretations. *Neuroimage*. 80:18.
- Lewis CM, Baldassarre A, Committeri G, Romani GL, Corbetta M. 2009. Learning sculpts the spontaneous activity of the resting human brain. *Proc Natl Acad Sci USA*. 106:17558–17563.
- Lord A, Horn D, Breakspear M, Walter M. 2012. Changes in community structure of resting state functional connectivity in unipolar depression. *PLoS ONE*. 7:e41282.
- Mantini D, Della Penna S, Marzetti L, de Pasquale F, Pizzella V, Corbetta M, Romani GL. 2011. A signal-processing pipeline for magnetoencephalography resting-state networks. *Brain Connectivity*. 1:49–59.
- Marzetti L, Della Penna S, Snyder AZ, Pizzella V, Nolte G, de Pasquale F, Romani GL, Corbetta M. 2013. Frequency specific interactions of MEG resting state activity within and across brain networks as revealed by the multivariate interaction measure. *Neuroimage*. 79:172–183.
- Maslov S, Sneppen K. 2002. Specificity and stability in topology of protein networks. *Science*. 296:910–913.
- McAuley JJ, da Fontoura Costa L, Caetano TS. 2007. The rich-club phenomenon across complex network hierarchies. *Appl Phys Lett*. 91:084103.
- Nir Y, Mukamel R, Dinstein I, Privman E, Harel M, Fisch L, Gelbard-Sagiv H, Kipervasser S, Andelman F, Neufeld MY, et al. 2008. Interhemispheric correlations of slow spontaneous neuronal fluctuations revealed in human sensory cortex. *Nat Neurosci*. 11:1100–1108.
- Nolte G, Bai O, Wheaton L, Mari Z, Vorbach S, Hallett M. 2004. Identifying true brain interaction from EEG data using the imaginary part of coherency. *Clin Neurophysiol*. 115:2292–2307.
- Power JD, Schlaggar BL, Lessov-Schlaggar CN, Petersen SE. 2013. Evidence for hubs in human functional brain networks. *Neuron*. 79:798–813.
- Rubinov M, Sporns O. 2010. Complex network measures of brain connectivity: uses and interpretations. *NeuroImage*. 52:1059–1069.
- Seber GAF, Wild CJ. 2003. Non linear regression. Hoboken (NJ): Wiley and Sons.
- Sestieri C, Shulman GL, Corbetta M. 2010. Attention to memory and the environment: functional specialization and dynamic competition in human posterior parietal cortex. *J Neurosci*. 30:8445–8456.
- Shanahan M. 2012. The brain's connective core and its role in animal cognition. *Philos Trans R Soc Lond B Biol Sci*. 367:2704–2714.
- Shirer WR, Ryali S, Rykhlevskaia E, Menon V, Greicius MD. 2012. Decoding subject-driven cognitive states with whole-brain connectivity patterns. *Cereb Cortex*. 22:158–165.
- Smith SM, Fox PT, Miller KL, Glahn DC, Fox PM, Mackay CE, Filippini N, Watkins KE, Toro R, Laird AR, et al. 2009. Correspondence of the brain's functional architecture during activation and rest. *Proc Natl Acad Sci USA*. 106:13040–13045.
- Sporns O. 2011. *Networks of the brain*. Cambridge (MA): The MIT Press.
- Stanley ML, Moussa MN, Paolini BM, Lyday RG, Burdette JH, Laurienti PJ. 2013. Defining nodes in complex brain networks. *Front Comput Neurosci*. 7:169.

- Tomasi D, Volkow ND. 2010. Functional connectivity density mapping. *Proc Natl Acad Sci USA*. 107:9885–9890.
- Tomasi D, Volkow ND. 2011. Functional connectivity hubs in the human brain. *Neuroimage*. 57:908–917.
- Van de Ville D, Britz J, Michel CM. 2010. EEG microstate sequences in healthy humans at rest reveal scale-free dynamics. *Proc Natl Acad Sci USA*. 107:18179–18184.
- van den Heuvel MP, Sporns O. 2013. An anatomical substrate for integration among functional networks in human cortex. *J Neurosci*. 33:14489–14500.
- Yeo BT, Krienen FM, Sepulcre J, Sabuncu MR, Lashkari D, Hollinshead M, Roffman JL, Smoller JW, Zollei L, Polimeni JR, et al. 2011. The organization of the human cerebral cortex estimated by intrinsic functional connectivity. *J Neurophysiol*. 106:1125–1165.
- Zalesky A, Fornito A, Cocchi L, Gollo LL, Breakspear M. 2014. Time-resolved resting-state brain networks. *Proc Natl Acad Sci USA*. 111:10341–10346.
- Zuo XN, Ehmke R, Mennes M, Imperati D, Castellanos FX, Sporns O, Milham MP. 2012. Network centrality in the human functional connectome. *Cereb Cortex*. 22:1862–1875.